INSTITUTO SUPERIOR TÉCNICO
Universidade Técnica de Lisboa

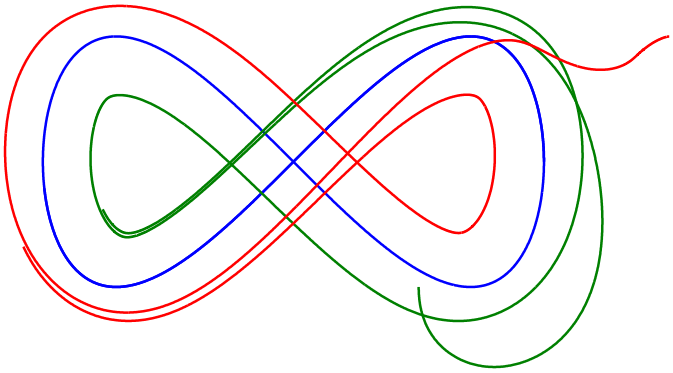

Formation Control of Autonomous Air Vehicles

Valter Roldrigues Roldão

Dissertação para a obtenção do Grau de Mestre em

Engenharia Aeroespacial

Júri

Presidente:	Professor Doutor João Manuel Lage de Miranda Lemos
Orientador:	Prof. Doutor Carlos Jorge Ferreira Silvestre
Co-orientador:	Prof. Doutor Paulo Jorge Coelho Ramalho Oliveira
Co-orientador:	Doutora Rita Maria Mendes de Almeida Correia da Cunha
Vogal:	Prof. Doutor Pedro Manuel Urbano Almeida Lima
Vogal:	Prof. Doutora Alexandra Moutinho

Outubro de 2012

Acknowledgments

This work would not have been possible without the contributions and support of countless people to whom I would like to express my sincere gratitude. In particular I would like to thank my supervisor and my co-supervisors for accepting me as their student and for guiding me throughout this thesis. I would also like to thank the jury for accepting to take part in the evaluation of this thesis.

I am grateful to all the members of DSOR I have had the opportunity to work with. I am especially grateful to David Cabecinhas and Bruno Cardeira, without whom the experimental part of this thesis would not have been possible.

Last but not least, to all my friends and family, who gave me support when I needed, who were with me all this time, I want to say thank you.

The work presented in this thesis was partly funded by Fundação para a Ciência e Tecnologia (FCT) under the Projects PEst-OE/EEI/LA0009/2011 and SCARVE-PTDC/EEA-CRO/102857/2008.

Resumo

A presente tese aborda o problema do movimento em formação de vários veículos autónomos. Uma nova estratégia baseada no conceito de seguimento de líder é proposta e os resultados de simulações e testes experimentais são apresentados e discutidos. A abordagem consiste em separar a coordenação em dois passos: um primeiro passo em que o movimento de um veículo, o líder, é passado a um planeador de trajectórias e um segundo em que as trajectórias geradas pelo planeador são passadas aos restantes veículos da formação.

Usando uma abordagem baseada em Lyapunov, o planeador prescreve o movimento a um grupo de veículos virtuais, modelados como uniciclos, por forma a manter o líder numa posição predefinida num referencial local. Através da restrição do movimento destes veículos, o planeador garante a geração de trajectórias de formação adequadas, evitando-se assim o recurso a parametrizações do caminho.

No segundo passo, as trajectórias descritas pelos veículos virtuais são passadas como referência aos veículos reais, neste caso, quadrotors. Por forma a testar o conceito apresentado em simulação, um modelo matemático do quadrotor é construído e um controlador para seguimento de trajectória desenhado. Por último, os resultados de testes experimentais realizados são apresentados, demonstrando o desempenho da solução proposta para a coordenação de veículos autónomos.

Palavras-chave: seguimento de líder, coordenação, quadrotor, controlo não-linear, backstepping

Abstract

This thesis addresses the problem of motion coordination between autonomous vehicles. A new strategy based on the concept of leader-following is proposed and results of experimental tests are presented. The approach consists in separating the coordination in two steps: a first step in which the motion of the leader is passed to a trajectory planner and a second step in which the trajectories generated by the planner are passed to the vehicles to be tracked.

Using a Lyapunov-based approach, the planner prescribes the motion for a group of virtual vehicles, modelled as unicycles, so as to keep the leader in a predefined configuration in their reference frame. By constraining the motion of these vehicles, the planner naturally guarantees the generation of adequate formation trajectories, bypassing the onerous task of obtaining path parametrizations.

In the second step, the trajectories of the virtual vehicles are used as reference trajectories to a group of real vehicles, in this case quadrotors. To test the concept in simulation a trajectory tracking controller is designed and a model of the plant derived. Finally, results of experimental tests are presented demonstrating the performance of the proposed solution for motion coordination of autonomous vehicles.

Keywords: leader-following, coordination, quadrotor, nonlinear control, backstepping

Contents

Acknowledgments . . . iii
Resumo . . . v
Abstract . . . vii
List of Tables . . . xi
List of Figures . . . xiv
List of Symbols . . . xvii

1 Introduction **1**
1.1 Motivation . . . 2
1.2 State-of-the-art . . . 2
1.3 Thesis Outline . . . 3
1.4 Notation . . . 4

2 Trajectory Planner **5**
2.1 Frames and Mappings . . . 5
2.2 Model . . . 7
2.3 Controller . . . 8
2.4 Inner Dynamics Analysis . . . 13
2.5 Results . . . 19
2.6 Trajectory planner . . . 22
2.6.1 Concept . . . 22
2.6.2 Three-dimensional trajectories . . . 23
2.6.3 Formation initialisation . . . 24
2.7 Summary . . . 24

3 Quadrotors in formation **27**
3.1 Quadrotor Model . . . 27
3.1.1 Kinematics . . . 27
3.1.2 Dynamics . . . 29
3.1.3 Aerodynamics . . . 30

3.1.4 Model Summary . . . 31
3.2 Quadrotor Trajectory Tracking Controller . . . 31
3.3 Results . . . 35
3.4 Summary . . . 41

4 Experimental Evaluation **43**
4.1 Experimental Set-up . . . 43
4.1.1 Quadrotor . . . 44
4.1.2 VICON System . . . 45
4.1.3 Acceleration estimation . . . 47
4.2 Results . . . 48
4.3 Discussion . . . 53

5 Conclusions **57**
5.1 Future Work . . . 58

A Trajectory Analysis **61**
A.1 Eight Trajectory . . . 62

B Quadrotor Controller – Complementary Mathematic **63**

List of Tables

3.1 Configuration parameters of the quadrotor controller. 36
3.2 Configuration parameters for the simulated flight formation. 38

4.1 Controller parameters used in the experimental tests. 48

List of Figures

2.1 Illustration of the vehicle moving in the 2D-Space. 7
2.2 Position of the leader in the inertial and in the follower's frames. 9
2.3 Regions where $\dot{V}_3 < 0$. 12
2.4 Points where $\dot{V}_\theta = 0$ 14
2.5 Trajectory described by the followers when d_x is two times the radius of the circumference described by the leader, but with different values of d_y. 15
2.6 Possible follower configurations for a leader tracking a circle. 15
2.7 Leader and followers describing coincident circles of radius R_0, with the same value of d_x but different d_y. 16
2.8 Evolution of $|\theta_d|_{\max}$ and of the bound of equation (2.34) with $|d_x \kappa_L|_{\max}$ left (L) and difference between the estimated and effective value of $|\theta_d|_{\max}$ on the right(R). . . 18
2.9 Position of leader and followers for the former stopped at $[0\ 0]^T$. 20
2.10 Time evolution of forward speed, angular speed and angular position of both followers. 20
2.11 Time evolution of the components of errors $\mathbf{e}_1$ and $\mathbf{e}_2$ of both followers. 21
2.12 Position of the leader and followers for the former describing an '8' with $\omega_N = 0.25\mathrm{rad/s}$ and $V_N = 0.5\mathrm{m/s}$. 21
2.13 Time evolution of forward speed, angular speed and angular position of both the followers. 21
2.14 Time evolution of the components of the errors $\mathbf{e}_1$ and $\mathbf{e}_2$ of both the followers. . . 22
2.15 Block diagram showing the leader-following strategy applied. 23

3.1 Diagram of a quadrotor and forces applied. 30
3.2 Trajectory described by the vehicle (blue), its attitude at initial moment and first 5 seconds, and the reference trajectory (red). 36
3.3 Controller errors over time. 37
3.4 Time evolution of linear (L) and angular (R) velocities. 37
3.5 Time evolution of thrust and desired thrust (L), and of torques (R). 37
3.6 Position of the quadrotors, generated trajectories and reference. 38
3.7 Velocity of the followers throughout the simulation. 39

3.8 Followers errors throughout the simulation. 39
3.9 Virtual followers errors throughout the simulation. 40
3.10 Sample trajectory generated (in this case for the second follower). 40
3.11 Time evolution of distance between leader and followers (and between them). . . . 41

4.1 System architecture. 44
4.2 Block Diagram of the Simulink model used. 44
4.3 The Blade® mQX quadrotor and its specifications. 45
4.4 The individual camera close-up and laboratory with the cameras installed there. . 46
4.5 A screenshot of the tracking software showing the cameras, their orientation and some vehicles at the centre. 46
4.6 Comparison of raw double differences (L) to smoothed with a MAv filter (R) applied to a sample circular trajectory 47
4.7 Position of the leader, generated trajectories and respective followers. 48
4.8 Time evolution of velocities of both the followers. 49
4.9 Time evolution of the errors for both the virtual followers. 49
4.10 Time evolution of controller errors for both the followers. 49
4.11 Time evolution of distance between leader and followers (and between them). . . . 50
4.12 Position of the leader, generated trajectories and respective followers. 51
4.13 Time evolution of velocities of both the followers. 51
4.14 Time evolution of errors for both the virtual followers. 51
4.15 Time evolution of controller errors for the both followers. 52
4.16 Time evolution of square reference trajectory (a complete track). 52
4.17 Position of the leader, generated trajectory and respective follower. 53
4.18 Time evolution of velocities and Euler angles of the follower. 53
4.19 Time evolution of errors for the virtual follower. 53
4.20 Time evolution of controller errors for the follower. 54

A.1 Evolution of κ_L for a nominal value of κ_N. 62

List of Symbols

Planner

$\mathbf{i}$, $\mathbf{j}$	Unit vectors of the canonical basis
$\mathbf{i}_{Fi}$, $\mathbf{j}_{Fi}$	Unit vectors of a follower's frame
$\{F_i\}$	Follower's i frame
$\{I\}$	Inertial frame
$\mathbf{p}_L$	Leader's position.
$\mathbf{p}_{Fi}$	Follower's i position.
ω	Follower's angular speed
$\mathcal{R}$	Rotation matrix of vectors in a generic follower's frame $\{F\}$ to inertial frame $\{I\}$.
θ	Follower's orientation angle
u	Follower's forward speed
τ	Follower's angular actuation [rad/s^2].
T	Vehicle thrust actuation [m/s^2].
$\mathbf{d}$	Goal position of the Leader in the Follower's frame.
$\mathbf{e}_1$, $\mathbf{e}_2$	Controller errors.
k_1, k_2	Controller gains.
$\boldsymbol{\mu}$	Actuation vector.
$\boldsymbol{\Gamma}$	Constant matrix that multiplies the actuation.
$\sigma(x)$	Saturation function.
σ_z	Vertical acceleration saturation function
$e_{\max}$	Maximum error to start the formation

$z_{\max}$ Maximum value of saturation function σ_z

κ_L Curvature of leader's trajectory

ω_L Leader's angular speed

V_L Leader's speed

ω_L Leader's angular speed

θ_L Leader's direction of movement

θ_d Difference between Leader's and Follower's direction of movement

$\mathbf{I}_2$ Identity matrix

Quadrotor

$\mathbf{i}$, $\mathbf{j}$, $\mathbf{k}$ Unit vectors of the canonical basis.

$\mathbf{i}_B$, $\mathbf{j}_B$, $\mathbf{k}_B$ Base vectors of quadrotor's body frame.

$\mathbf{r}_i$ Rotation matrix i^{th} column

$\{B\}$ Vehicle's body reference frame

$\{I\}$ Inertial reference frame

$\boldsymbol{\omega}$ Quadrotor's angular velocity relative to $\{I\}$ and written in $\{B\}$

$\boldsymbol{\tau}$ Torque input transformation

ψ, θ, ϕ Euler angles describing body's attitude (yaw, pitch, and roll, respectively)

$\mathcal{R}$ Rotation matrix of vectors in $\{B\}$ to $\{I\}$

$\mathbf{J}$ Quadrotor tensor of inertia

$\mathbf{n}$ Quadrotor torque input

$\mathbf{p}$ Quadrotor's position

$\mathbf{v}$ Quadrotor's velocity relative to $\{I\}$ and written in $\{B\}$

g Gravitational acceleration

m Quadrotor mass

T Quadrotor total thrust

$\mathbf{r}_{3d}$ Desired thrust direction

$\sigma_{\max}$	Maximum value of $\boldsymbol{\sigma}_e$
$\boldsymbol{\sigma}_e$	Errors $\mathbf{e}_1$ and $\mathbf{e}_2$ saturation function
$\mathbf{e}_i$	Quadrotor controller errors, $i \in \{1, 2, 3, 4\}$
$\mathbf{p}_d$	Quadrotor desired position
k_i	Quadrotor controller gains, $i \in \{1, 2, 3, 4\}$
Q, P	Positive definite weight matrices used in controller development
T_d	Desired thrust
$W_i(\cdot)$	Quadratic function of its arguments
θ_{ref}	Planar projection of direction of reference trajectory
$\mathbf{p}_{Fi}$	Position of follower i
$\mathbf{p}_{ref}$	Reference trajectory
$\mathbf{I}_3$	Identity matrix
$\mathbf{S}(.)$	External product matrix ($\mathbf{S}(\mathbf{x})\mathbf{y} = \mathbf{x} \times \mathbf{y}$)

Chapter 1

Introduction

The propensity to aggregation and swarming is a behaviour extensively common in biology. From atoms that group together to form chemical compounds, to insects that live in colonies, and to flocks of birds in migration, among others, there is a variety of examples of grouping behaviour reported in nature. While it is not totally understood, it is accepted that swarming is advantageous in terms of surviving expectancy and reproductive effectiveness (see for example [1]). It is also advantageous in terms of efficiency for migrating birds – studies have been made demonstrating a reduction of 20% in energy consumption for a flock of geese flying in a 'V' configuration when compared to the solitary flight [2].

Nature has since ever inspired human inventions and, in the last decades, great attention has been given to the swarm behaviour of certain animals, its positive outcomes, and how these kind of synergies might be exploited in robot coordination. Several strategies taking advantage of robot coordination have been studied in fields that range from underwater [3], to aerial [4], or spacial [5] [6].

A growing interest is given to taking advantage of robot coordination for area exploration and surveillance. The basic principle is that each entity of the swarm contributes with its sensing to the knowledge of the group resulting in a faster and more efficient process. The authors of [7] propose an approach for area exploration based on multi-robot coordination with limited communication range capabilities. In [4], a strategy for mapping using a network of distributed UAV (Unmanned Air Vehicle) is proposed. Several examples may also be found unveiling the interest that has been given to using swarms of UAVs for surveillance and target detection (see for example [8], [9], [10] or [11]). In [12] a comparison between coordinated and non-coordinated target search and identification is established, showing that coordination leads to faster target identification.

One other example in which the use of multiple plants may be advantageous is in the transportation of large objects (see e.g. [13]). The use of multiple plants makes it possible to transport heavier loads and to control their attitude even using towing cables, which is not possible to do with an isolated plant. An approach to moving polygon-like loads on the ground in environments

with obstacles is developed in [14]. A more demanding situation is the transportation of a cable suspended load by a group of quadrotors, which is proposed and tested in [15].

1.1 Motivation

In most of the examples of cooperation presented above synchronisation of movements has a positive outcome. Such is the case of area exploration, for instance, where a thoughtful distribution of robots may reduce the overlap of fields-of-view, thus maximising the area explored. In other cases, synchronisation may be a requirement for the correct execution of the task, which is the case of load transportation, for example.

Although there are many approaches to robot synchronisation, they can be aggregated into two major groups. The strategies that do not control vehicles organisation and whose only objective is to promote aggregation of vehicles while guaranteeing that each keeps a minimum distance from its neighbours (see e.g. [16], [17], or [18]); and the strategies that are capable of maintaining a fixed robot configuration (see for example [19]). Using these strategies, each robot is driven to a pre-assigned relative position within the formation with respect to other vehicles. These configurations are fixed from the view point of a fixed observer, irrespectively of the direction of movement.

For the execution of some tasks, however, it might be advantageous to keep a fixed configuration with respect to the direction of movement. Extensive studies carried out showed a reduction of induced drag for aircrafts flying in a V configuration (see e.g. [20] and [21]). This kind of fixed configurations is also of interest for military flight missions as they allow for continuous visual contact [22].

1.2 State-of-the-art

Most of the work concerning robot formation was developed in the past ten to fifteen years. The majority employ the idea of potential fields to drive the vehicles of the swarm to a desired distance from one another.

The authors of [17] developed a strategy for planar formations using the planar Frenet-Serret equations of motion to describe the trajectories. The concept can be explained as follows: charged particles move at constant speed in a two dimensional space and are affected by a magnetic field whose intensity is the control input, varying depending on a potential field generated by the neighbouring vehicles. Example trajectories of leader-following simulations presented show richness of behaviours. However, the complexity of the design makes the algorithm computational expensive. Formal proof of stability is provided for the case of two vehicles. On the other hand, for an arbitrary number of vehicles only a characterization of the possible stability is provided. In [18] an extension of the foregoing strategy is presented, where obstacle avoidance

and splitting and regrouping capabilities are introduced.

In an article presented in 2001, [23], Leonard and Fiorelli proposed the use of potential fields associated with moving reference points, which they called *virtual leaders*, whose function is to shape and give reference movement to the formation. The vehicles are modelled as point particles and their actuation result from superposition of the potentials originated by their neighbours (including virtual leaders). With this strategy it is possible to control the shape and orientation of the formation by proper positioning the virtual leaders, although generating their trajectories may be difficult. Formal proof of global asymptotic stability is provided using a total energy function (kinetic and potential) as Lyapunov function.

The use of potentials to attract/repulse a vehicle towards/from its neighbours is also exploited in [16]. As in the foregoing solution, vehicles are modelled by point particles whose movement is influenced by the movement of their neighbours. They define an adjacency criterion so that only the vehicles within a circle of predefined radius are considered as neighbours, thus reducing the complexity of the control law. To guarantee cohesiveness of the swarm the control law is extended to include a term of attraction to the centre of mass of the formation. Obstacle avoidance is developed for planar formations by attaching virtual vehicles to their surface which produce repulsive forces. Simulation results show that the algorithm is effective in promoting swarming and collective movement behaviours. However, this approach cannot be employed in situations where a definite geometric configuration for the formation is of interest.

Guerrero *et al.* developed a strategy for coordinated flight of quadrotors [19]. They designed an integrated control law that stabilises the plants and allows them to follow a leader while maintaining a fixed configuration. The geometric configuration, though, is fixed from the point of view of a fixed observer and do not rotate according to the direction of movement. Although in concept rotation may be induced by reconfiguring the formation as it moves, it may originate unexpected transient behaviours.

1.3 Thesis Outline

Apart from introduction and conclusion, the present thesis is constituted by three chapters.

Chapter 2 is dedicated to the presentation of the designed strategy for motion coordination. A description of the vehicle model is provided followed by the derivation of the control law. Simulation results and respective discussion are also included.

Chapter 3 presents the developed concept to flight coordination applied to quadrotors. The plant model is described and a control law for trajectory tracking is designed. The concept was tested in simulation and the results and respective discussion appear in the end of the chapter.

Lastly, chapter 4 contains the experimental part of the work. The set-up is described and the obtained results are presented and discussed.

Each of these chapters include an introductory paragraph to aid the reader throughout. In the end of the text the reader may find some appendices which give complementary information.

1.4 Notation

Using consistent notation throughout a text is of key importance for its clarity. The following set of rules is applicable to every symbol presented in this text.

- Scalar values are represented by either upper or lower case letters (e.g. b and A);
- Vectors are represented in bold and lower case letters (e.g. $\mathbf{v}$);
- Matrices are represented in bold and upper case letters (e.g. $\mathbf{A}$);
- Frames are represented using upper case letters enclosed in curly brackets (e.g. $\{I\}$);
- Leading superscripts are used to identify the frame to which the quantity is relative (e.g. ${}^{I}\mathbf{d}$)
- Subscripts x, y and z are used to indicate the components of a vector (e.g. $\mathbf{v} = [v_x \;\; v_y \;\; v_z]^T$);
- Other subscripts are used to specify what the letter is referring to (e.g. $\mathbf{v_L}$ refers to leader's velocity);
- Vectors written in $\{B\}$ can be translated to $\{A\}$ by left multiplying by ${}^{A}_{B}\mathbf{R}$.
- Two superscripts on the left side indicate that the quantity is relative to one frame and written in the other (e.g. quantity $\mathbf{v}$ relative to $\{B\}$ and written in $\{A\}$: ${}^{A}({}^{B}\mathbf{v})$)

Chapter 2

Trajectory Planner

The trajectory planner is the centrepiece of the proposed strategy for formation control. As mentioned before, the planner is composed of a group of virtual vehicles that move with the objective of maintaining the leader in a predefined position with respect to a local frame. The model of the virtual vehicles is presented in section 2.2. The control law designed to comply with the objective set is described in section 2.3. Section 2.4 is dedicated to an analysis of the inner dynamics of the closed loop, while section 2.5 presents the results of a simulation conducted to assess the performance of the control law. The structure of the trajectory planner is presented in section 2.6.

2.1 Frames and Mappings

For the purpose of deriving a model for the following vehicles and designing a control law, it is required to introduce some frames. Each of these frames is composed of two orthogonal and unitary vectors forming an orthonormal basis of the two-dimensional Euclidean space. These frames are defined as follows:

inertial frame The frame $\{I\}$ is an orthogonal fixed frame defined by the set of unitary vectors $\{\mathbf{i}_I, \mathbf{j}_I\}$, such that $\mathbf{i}_I \cdot \mathbf{j}_I = 0$ and $i_{Ix} j_{Iy} - i_{Iy} j_{Ix} = 1$.

The Follower i frame The frames $\{F_i\}$, with $i \in \mathbb{N}$, are orthogonal frames defined by the set of unitary vectors $\{\mathbf{i}_{F_i}, \mathbf{j}_{F_i}\}$ with $\mathbf{i}_{F_i}$ aligned with the follower's direction of movement and $\mathbf{j}_{F_i}$ such that $\mathbf{i}_{F_i} \cdot \mathbf{j}_{F_i} = 0$ and $i_{F_i x} j_{F_i y} - i_{F_i y} j_{F_i x} = 1$.

For easiness of reading the subscript/superscript I in the base vectors will be omitted. Also, in base vectors with the same subscripts and superscripts these two will be omitted, since base vectors written in their own frames are equal to the canonical base vectors $\{\mathbf{i} = [1 \quad 0]^T, \mathbf{j} = [0 \quad 1]^T\}$.

Mapping between frames Any point described in one frame (e.g. $\{B\}$) can be described in another (e.g. $\{A\}$) using a map between those two frames, an element of the special Euclidean group, $({}^A_B\mathbf{R}, {}^A\mathbf{p}_B) \in SE(2)$. The matrix ${}^A_B\mathbf{R}$ is a rotation matrix and respects the following set of properties:

- A rotation matrix is a map between vectors written in two different frames (e.g. ${}^A\mathbf{u} = {}^A_B\mathbf{R}\,{}^B\mathbf{u}$);
- The determinant of a rotation matrix equals 1;
- The inverse of a rotation matrix is its transpose and therefore ${}^A_B\mathbf{R}^T\,{}^A_B\mathbf{R} = \mathbf{I}_2$, where $\mathbf{I}_2$ represents the identity matrix;
- The matrix of rotation from $\{B\}$ to $\{A\}$ is the inverse of the matrix of rotation from $\{A\}$ to $\{B\}$: ${}^A_B\mathbf{R}^T = {}^B_A\mathbf{R}$;
- Any rotation matrix can be obtained through the product of the unitary vectors which define the two frames, e.g.

$$ {}^A_B\mathbf{R} = \begin{bmatrix} \mathbf{i}_A \cdot \mathbf{i}_B & \mathbf{i}_A \cdot \mathbf{j}_B \\ \mathbf{j}_A \cdot \mathbf{i}_B & \mathbf{j}_A \cdot \mathbf{j}_B \end{bmatrix} = \begin{bmatrix} {}^A\mathbf{i}_B & {}^A\mathbf{j}_B \end{bmatrix} \tag{2.1} $$

  A rotation matrix can be parametrised by a variable ${}^A\theta_B = -{}^B\theta_A$ that represents the angular displacement between two frames.

$$ {}^A_B\mathbf{R} = \begin{bmatrix} \cos{}^A\theta_B & -\sin{}^A\theta_B \\ \sin{}^A\theta_B & \cos{}^A\theta_B \end{bmatrix} \tag{2.2} $$

- The derivative of a rotation matrix is given by

$$ \begin{aligned} {}^A_B\dot{\mathbf{R}} &= \begin{bmatrix} -\sin{}^A\theta_B & -\cos{}^A\theta_B \\ \cos{}^A\theta_B & -\sin{}^A\theta_B \end{bmatrix} {}^A\omega_B \\ &= \begin{bmatrix} \cos{}^A\theta_B & -\sin{}^A\theta_B \\ \sin{}^A\theta_B & \cos{}^A\theta_B \end{bmatrix} \begin{bmatrix} 0 & -{}^A\omega_B \\ {}^A\omega_B & 0 \end{bmatrix} \\ &= {}^A_B\mathbf{R}\mathbf{S}\left({}^A\omega_B\right) \end{aligned} \tag{2.3} $$

  where ${}^A\omega_B$ represents the angular speed of frame $\{B\}$ with respect to $\{A\}$, that is, the time derivative of ${}^A\theta_B$. The matrix $\mathbf{S}(x)$ is a skew-symmetric matrix of its argument.

The vector ${}^A\mathbf{p}_B$ represents the position of the origin of frame $\{B\}$ written in frame $\{A\}$. A point described in frame $\{B\}$ can be expressed in $\{A\}$ by

$$ {}^A\mathbf{p}_a = {}^A\mathbf{p}_B + {}^A_B\mathbf{R}\,{}^B\mathbf{p}_a \tag{2.4} $$

In most part of the coming sections only the inertial frame $\{I\}$ and a generic follower frame $\{F\}$, and the corresponding matrix of rotation ${}^I_F\mathbf{R}$, are used. Thus, consider the following simplified notation:

$$\begin{aligned} \theta &= {}^I\theta_F \\ \omega &= {}^I\omega_F \\ \mathcal{R} &= {}^I_F\mathbf{R} \end{aligned} \tag{2.5}$$

In case it is necessary to use any other frame, the former, more general, notation shall be used. Notice that the superscript I, present in variables written in the inertial frame, was dropped. Quantities written in other frames will still keep their frame's superscript, unless otherwise mentioned.

2.2 Model

Consider that each of the followers is modelled by a nonholonomic vehicle that can move forward and backward and rotate but cannot move sideways and do not slip [24]. Such vehicle is similar to a four wheeled car which wheels can move independently in pairs but cannot steer.

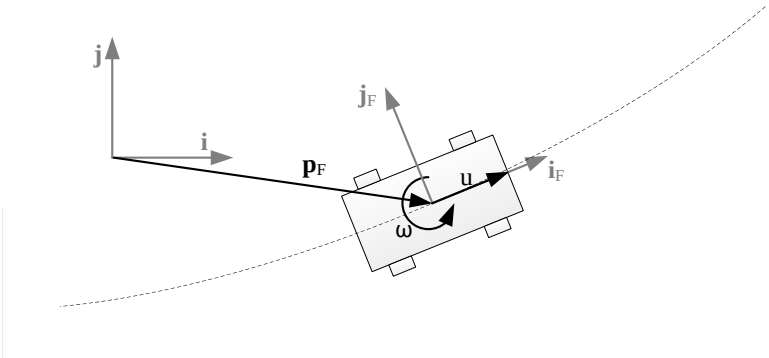

Figure 2.1: Illustration of the vehicle moving in the 2D-Space.

The velocity of a generic follower written in the inertial frame is given by

$$\dot{\mathbf{p}}_F = \mathcal{R}\begin{bmatrix} u \\ 0 \end{bmatrix} = \mathcal{R}\mathbf{i}u \tag{2.6}$$

or

$$\dot{\mathbf{p}}_F = \begin{bmatrix} \cos\theta \\ \sin\theta \end{bmatrix} u$$

where u is the forward speed of the car. Together with $\dot{\theta} = \omega$, these define the kinematic model of the unicycle, whose inputs are the forward and angular speeds. These equations cannot assume arbitrary values since they must verify the nonholonomic constraint [25]

$$\begin{bmatrix} \sin\theta & -\cos\theta & 0 \end{bmatrix} \begin{bmatrix} \dot{p}_{F\,x} \\ \dot{p}_{F\,y} \\ \dot{\theta} \end{bmatrix} = 0 \tag{2.7}$$

which intuitively is equivalent to restrain the lateral movement.

The model is extended to include the linear and angular speeds' derivatives which are necessary in later use. Computing the time derivative of equation (2.6) yields the acceleration in the inertial frame $\{I\}$.

$$^{I}\ddot{\mathbf{p}}_F = \mathcal{R}\mathbf{i}T + \mathcal{R}\mathbf{S}(\omega)\mathbf{i}u \tag{2.8}$$

with T being the actuation in the forward direction. Similarly, let the angular acceleration $\dot{\omega}$ be the other actuation, given by the variable τ.

$$\dot{\omega} = \tau$$

The following set of equations summarises the model of the follower vehicles.

$$\begin{aligned} \dot{\mathbf{p}}_F &= \mathcal{R}\mathbf{i}u \\ \ddot{\mathbf{p}}_F &= \mathcal{R}\mathbf{i}T + \mathcal{R}\mathbf{S}(\omega)\mathbf{i}u \\ \dot{\mathcal{R}} &= \mathcal{R}\mathbf{S}(\omega) \\ \dot{u} &= T \\ \dot{\omega} &= \tau \end{aligned} \tag{2.9}$$

2.3 Controller

The present control law was derived using the *backstepping* procedure. Although quite recent – the earlier works describing explicitly the procedure are not older than 20 years [26] – it has become very popular and one of the most used tools to derive nonlinear controllers. The procedure is synthetically described in a lecture given by one of its developers, Kokotović, in 1992 [27]:

> *"The key idea of backstepping is to start with a system which is stabilizable with a known feedback law for a known Lyapunov function, and then to add to its input an integrator. For the augmented system a new stabilizing feedback law is explicitly designed and shown to be stabilizing for a new Lyapunov function, and so on..."*

Consider a world composed of two vehicles. One is called leader and is describing a trajectory

that can be characterised at any moment by its position, velocity and acceleration – $\{\mathbf{p}_L, \dot{\mathbf{p}}_L, \ddot{\mathbf{p}}_L\}$. The other is called follower and its objective is to follow the leader and to move in a way as to maintain the leader in a fixed position in its own frame $\{F\}$. Figure 2.2 depicts the position of the leader as seen from the inertial frame ($\mathbf{p}_L$) and in the follower's point of view ($^F\mathbf{p}_L$).

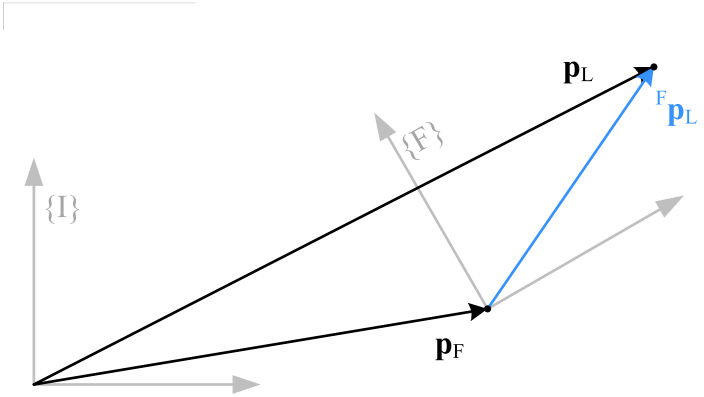

Figure 2.2: Position of the leader in the inertial and in the follower's frames.

Given a constant vectorial distance $\mathbf{d} = [d_x \quad d_y]^T$, the goal of the control law is to bring the follower to a configuration in which it sees the leader in a position $\mathbf{d}$ in its own frame $\{F\}$. Towards that end, let $\mathbf{e}_1$ be the position error, given by

$$\mathbf{e}_1 = {}^F\mathbf{p}_L - \mathbf{d} = \mathcal{R}^T \left(\mathbf{p}_L - {}^I\mathbf{p}_F\right) - \mathbf{d} \tag{2.10}$$

Computing the time derivative of $\mathbf{e}_1$ one arrives at

$$\begin{aligned}
\dot{\mathbf{e}}_1 =& \dot{\mathcal{R}}^T \left(\mathbf{p}_L - \mathbf{p}_F\right) + \mathcal{R}^T \left(\dot{\mathbf{p}}_L - \dot{\mathbf{p}}_F\right) \\
=& -\mathbf{S}(\omega)\mathcal{R}^T \left(\mathbf{p}_L - \mathbf{p}_F\right) + \mathcal{R}^T \left(\dot{\mathbf{p}}_L - \mathcal{R}\mathbf{i}u\right) \\
=& -\mathbf{S}(\omega)\, {}^F\mathbf{p}_L + \mathcal{R}^T \left(\dot{\mathbf{p}}_L - \mathcal{R}\mathbf{i}u\right) \\
=& -\mathbf{S}(\omega) \left(\mathbf{e}_1 + \mathbf{d}\right) + \mathcal{R}^T\dot{\mathbf{p}}_L - \mathbf{i}u
\end{aligned} \tag{2.11}$$

To start the backstepping procedure, consider a first Lyapunov candidate function given by:

$$V_1 = \frac{1}{2}\mathbf{e}_1^T\mathbf{e}_1 \tag{2.12}$$

Evaluation of its temporal derivative yields

$$\begin{aligned}
\dot{V}_1 =& \mathbf{e}_1^T\dot{\mathbf{e}}_1 \\
=& \mathbf{e}_1^T \left[-\mathbf{S}(\omega) \left(\mathbf{e}_1 + \mathbf{d}\right) + \mathcal{R}^T\dot{\mathbf{p}}_L - u\mathbf{i}\right] \\
=& \mathbf{e}_1^T \left[-\mathbf{S}(\omega)\mathbf{d} + \mathcal{R}^T\dot{\mathbf{p}}_L - u\mathbf{i}\right]
\end{aligned}$$

The mathematical property $\mathbf{x}^T\mathbf{S}(y)\mathbf{x} = 0$ was used to eliminate $\mathbf{e}_1^T\mathbf{S}(\omega)\mathbf{e}_1$. Now, summing and subtracting a term $k_1\mathbf{e}_1^T\boldsymbol{\sigma}(\mathbf{e_1})$ to $\dot{V}_1$ and rearranging the terms to make the first part of the equation negative definite, $\dot{V}_1$ becomes

$$\dot{V}_1 = -k_1\mathbf{e}_1^T\boldsymbol{\sigma}(\mathbf{e_1}) + k_1\mathbf{e}_1^T\left[\boldsymbol{\sigma}(\mathbf{e_1}) + \frac{1}{k_1}\left(-\mathbf{S}(\omega)\mathbf{d} + \mathcal{R}^T\dot{\mathbf{p}}_L - u\mathbf{i}\right)\right]$$

The function $\boldsymbol{\sigma}(\mathbf{e_1})$ is a saturation function included in order to limit the influence of the position error in the actuation and is given by

$$\boldsymbol{\sigma}(\mathbf{e_1}) = p_{\max}\tanh\left(\mathbf{x}/p_{\max}\right) \tag{2.13}$$

where the parameter $p_{\max}$ is a configurable constant.

Declaring a new error $\mathbf{e}_2$ given by

$$\mathbf{e}_2 = \boldsymbol{\sigma}(\mathbf{e_1}) + \frac{1}{k_1}\left(-\mathbf{S}(\omega)\mathbf{d} + \mathcal{R}^T\dot{\mathbf{p}}_L - u\mathbf{i}\right) \tag{2.14}$$

allows $\dot{V}_1$ to be rewritten in the following compact form:

$$\dot{V} = -k_1\mathbf{e}_1^T\boldsymbol{\sigma}(\mathbf{e_1}) + k_1\mathbf{e}_1^T\mathbf{e}_2$$

Consider a second Lyapunov candidate function which is created to include the new error $\mathbf{e}_2$.

$$V_2 = \frac{1}{2}\sum_{i=1}^{2}\mathbf{e_i}^T\mathbf{e_i} \tag{2.15}$$

Evaluation of its time derivative yields

$$\begin{aligned}
\dot{V}_2 &= \dot{V}_1 + \mathbf{e}_2^T\dot{\mathbf{e}}_2 \\
&= \dot{V}_1 + \mathbf{e}_2^T\left[\dot{\boldsymbol{\sigma}}(\mathbf{e_1}) + \frac{1}{k_1}\left(-\mathbf{S}\left(\dot{\omega}\right)\mathbf{d} - \mathbf{S}(\omega)\mathcal{R}^T\dot{\mathbf{p}}_L + \mathcal{R}^T\ddot{\mathbf{p}}_L - \mathbf{i}T\right)\right] \\
&= \dot{V}_1 + \mathbf{e}_2^T\left[\dot{\boldsymbol{\sigma}}(\mathbf{e_1}) + \frac{1}{k_1}\left(-\mathbf{S}(\tau)\mathbf{d} - \mathbf{S}(\omega)\mathcal{R}^T\dot{\mathbf{p}}_L + \mathcal{R}^T\ddot{\mathbf{p}}_L - \mathbf{i}T\right)\right] \\
&= \dot{V}_1 + \frac{1}{k_1}\mathbf{e}_2^T\left(k_1\dot{\boldsymbol{\sigma}}(\mathbf{e_1}) - \begin{bmatrix}1 & -d_y \\ 0 & d_x\end{bmatrix}\begin{bmatrix}T \\ \tau\end{bmatrix} - \mathbf{S}(\omega)\mathcal{R}^T\dot{\mathbf{p}}_L + \mathcal{R}^T\ddot{\mathbf{p}}_L\right)
\end{aligned} \tag{2.16}$$

The algebraic manipulation carried out in the last step made it possible to concentrate the vehicle's actuation in only one vector, multiplied by a constant matrix, which is invertible for $d_x \neq 0$. For a

more compact writing consider the following definitions:

$$\mathbf{\Gamma} = \begin{bmatrix} 1 & -d_y \\ 0 & d_x \end{bmatrix} \tag{2.17}$$

$$\boldsymbol{\mu} = \begin{bmatrix} T \\ \tau \end{bmatrix} \tag{2.18}$$

$$\boldsymbol{\delta} = -\mathbf{S}(\omega)\mathcal{R}^T\dot{\mathbf{p}}_L + \mathcal{R}^T\ddot{\mathbf{p}}_L \tag{2.19}$$

In order to force the convergence of the errors even in the presence of any perturbation, an integral state is introduced.

$$\dot{\boldsymbol{\xi}} = \mathbf{e}_2 \tag{2.20}$$

The choice for using $\mathbf{e}_2$ instead of $\mathbf{e}_1$ in the integral state is given to the fact that it provides in general better stability results than the alternative, as suggested in [28].

Consider a new Lyapunov candidate function given by

$$V_3 = V_2 + \frac{k_3}{2}\boldsymbol{\xi}^T\boldsymbol{\xi} \tag{2.21}$$

The time derivative of V_3 is given by

$$\begin{aligned} \dot{V}_3 =& \dot{V}_2 + k_3\boldsymbol{\xi}^T\mathbf{e}_2 \\ =& \dot{V}_1 + \frac{\mathbf{e}_2^T}{k_1}\left(k_1\dot{\boldsymbol{\sigma}}(\mathbf{e_1}) + \boldsymbol{\delta} + k_1k_3\boldsymbol{\xi} - \mathbf{\Gamma}\boldsymbol{\mu}\right) \end{aligned} \tag{2.22}$$

As a control law for $\boldsymbol{\mu}$, consider

$$\boldsymbol{\mu} = \Gamma^{-1}\left(\boldsymbol{\delta} + k_1\dot{\boldsymbol{\sigma}}(\mathbf{e_1}) + k_1^2k_2\mathbf{e}_2 + k_1k_3\boldsymbol{\xi}\right) \tag{2.23}$$

which is well defined for any $d_x \neq 0$.

At this point, it is possible to state the following result.

Theorem 2.1. *Consider the simplified vehicle model described in equation* (2.9) *and the error system consisting of the errors* $\mathbf{e}_1$ (2.10) *and* $\mathbf{e}_2$ (2.14)*. The control law*

$$\boldsymbol{\mu} = \Gamma^{-1}\left(\boldsymbol{\delta} + k_1\dot{\boldsymbol{\sigma}}(\mathbf{e_1}) + k_1^2k_2\mathbf{e}_2 + k_1k_3\xi\right) \tag{2.24}$$

with $k_1 > 0$*,* $k_2 > 1$*, and* $k_3 > 0$*, makes the origin of the error system globally and asymptotically stable.*

Proof. Substituting $\boldsymbol{\mu}$ into $\dot{\mathbf{e}}_2$ it becomes

$$\dot{\mathbf{e}_2} = -\boldsymbol{\Gamma}\boldsymbol{\mu} + \boldsymbol{\delta} + \dot{\boldsymbol{\sigma}}(\mathbf{e_1}) = -k_1k_2\mathbf{e}_2 - k_1k_3\boldsymbol{\xi}$$

being possible to write the following system of equations

$$\dot{\mathbf{x}} = \begin{bmatrix} \dot{\mathbf{e}}_2 \\ \dot{\boldsymbol{\xi}} \end{bmatrix} = - \begin{bmatrix} 0 & -1 \\ k_1k_3 & k_1k_2 \end{bmatrix} \begin{bmatrix} \mathbf{e}_2 \\ \boldsymbol{\xi} \end{bmatrix} \tag{2.25}$$

For $k_i > 0$, the origin of (2.25) is globally exponentially stable, which implies that there exist positive scalars λ and α such that

$$\|\mathbf{x}\| \leq a\|\mathbf{x}(0)\|e^{-\lambda t}$$

To prove that the origin is asymptotically stable consider the substitution of equation (2.23) into (2.22) yielding

$$\begin{aligned} \dot{V}_3 =& - k_1\mathbf{e}_1^T\boldsymbol{\sigma}(\mathbf{e_1}) + k_1\mathbf{e}_1^T\mathbf{e}_2 - k_1k_2\mathbf{e}_2^T\mathbf{e}_2 \\ \leq& - k_1\|\mathbf{e}_1\|\|\boldsymbol{\sigma}(\mathbf{e_1})\| + k_1\|\mathbf{e}_1\|\|\mathbf{e}_2\| - k_1k_2\|\mathbf{e}_2\|^2 \end{aligned}$$

which is negative whenever either $\|\mathbf{e}_2\| \leq \|\boldsymbol{\sigma}(\mathbf{e_1})\|$ or $\|\mathbf{e}_1\| \leq k_2\|\mathbf{e}_2\|$ is verified (see figure 2.3). If $k_2 > 1$, then there exists $\|\mathbf{e}_1\| > 0$ for which $\|\mathbf{e}_1\| = k_2\|\boldsymbol{\sigma}(\mathbf{e}_1)\| = k_2c$. Whenever $\|\mathbf{e}_2\| \leq c$, $\dot{V}_3$ is negative semi-definite.

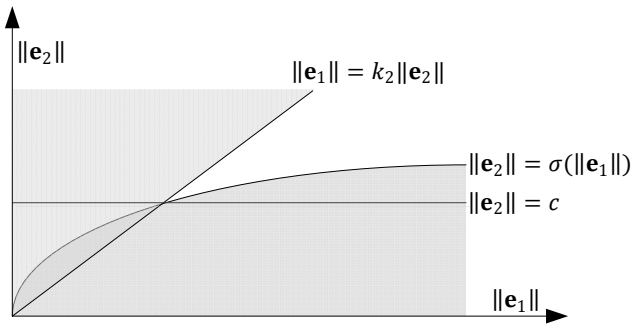

Figure 2.3: Regions where $\dot{V}_3 < 0$.

Since $\|\mathbf{e}_2\| \leq \|\mathbf{x}\| \leq \alpha\|\mathbf{x}(0)\|e^{-\lambda t}$, there is a time t_1 when, for $t > t_1$, $\dot{V}_3$ becomes negative semi-definite. Since the error systems is autonomous, we can apply LaSalle's Invariance Principle to conclude that the origin is globally asymptotically stable.

□

2.4 Inner Dynamics Analysis

Having the error system stable do not imply the intrinsic variables of the vehicle to be stable. For a given leader's position and a given $\mathbf{d}$ there are infinite solutions for the follower's state satisfying the condition $\mathbf{e}_1 = 0$, which indicates the existence of a zero dynamics, whose stability needs to be analysed. Towards that end, consider the limit condition when the errors have converged to zero. In that situation it is possible to write:

$$\begin{bmatrix} u \\ \dot{\theta} \end{bmatrix} = \mathbf{\Gamma}^{-1}\mathcal{R}^T\dot{\mathbf{p}}_L \tag{2.26}$$

Defining $\dot{\mathbf{p}}_L$ as

$$\dot{\mathbf{p}}_L = V_L \begin{bmatrix} \cos\theta_L \\ \sin\theta_L \end{bmatrix} \tag{2.27}$$

with V_L and θ_L continuous functions representing the norm and direction of movement of the leader, respectively. Using these definitions, equation (2.26) can be rearranged into the form

$$\begin{bmatrix} u \\ \dot{\theta} \end{bmatrix} = \begin{bmatrix} V_L\cos(\theta_L - \theta) + \dfrac{V_L d_y}{d_x}\sin(\theta_L - \theta) \\ \dfrac{V_L}{d_x}\sin(\theta_L - \theta) \end{bmatrix} \tag{2.28}$$

It is worth noting that the second equation has solely one variable, θ (apart from the inputs), and that it does not depend on d_y.

Let θ_d be the angle given by $\theta - \theta_L$. The time derivative of θ_d is given by

$$\dot{\theta}_d = -\frac{V_L}{d_x}(\sin\theta_d + d_x\kappa_L) \tag{2.29}$$

with, κ_L being the trajectory curvature, given by quotient of ω_L and V_L, which can be seen as the inverse of the instantaneous radius of rotation of the trajectory. The analysis will now be divided in two cases, the first case corresponding to trajectories with $\dot{\kappa}_L = 0$, the second to trajectories with $\dot{\kappa}_L \neq 0$.

When $\dot{\kappa}_L = 0$ Trajectories with $\dot{\kappa}_L = 0$ can be either a circumference, when $\kappa_L \neq 0$, or a line, otherwise. For this type of trajectories it is possible to prove their stability. Towards that end consider the candidate *Lyapunov* function

$$V_\theta = \frac{1}{2}(\sin\theta_d + d_x\kappa_L)^2 \tag{2.30}$$

whose time derivative is given by

$$\begin{aligned}\dot{V}_\theta &= (\sin\theta_d + d_x\kappa_L)\,\dot{\theta}_d\cos\theta_d \\ &= -\frac{V_L}{d_x}\cos\theta_d\,(\sin\theta_d + d_x\kappa_L)^2 \\ &= -2\frac{V_L}{d_x}\cos\theta_d\,V_\theta\end{aligned}$$

which is zero for $\theta_d = \pm\pi/2$ and for $\sin\theta_d = -d_x\kappa_L$. Analysing the stability of these points it can be seen that:

$\boldsymbol{\theta_d = \pm\pi/2}$
Saddle points.

$\boldsymbol{\theta_d = -\arcsin(d_x\kappa_L)}$
Stable equilibrium point.

$\boldsymbol{\theta_d = \pi + \arcsin(d_x\kappa_L)}$
Unstable equilibrium point.

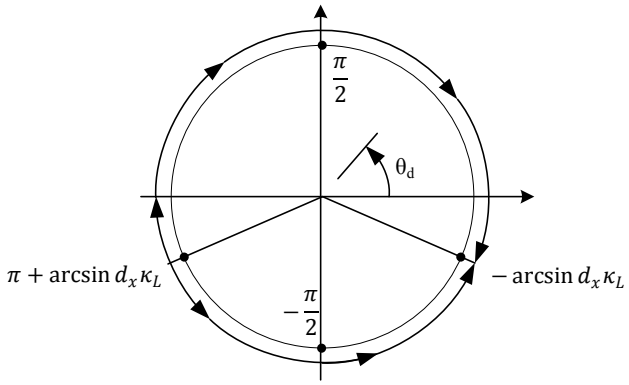

Figure 2.4: Points where $\dot{V}_\theta = 0$

From the above it can be concluded that there is only one stable value of θ_d for any pair d_x and κ_L. It can also be seen that no solution can be found for $|d_x\kappa_L| > 1$. For the case of a circular trajectory, this is equivalent to having d_x greater than the radius of the circumference described by the leader, $d_x > r_L$. In such situation θ_d do not converge and the trajectory described by the follower differs totally from the trajectory described by the leader.

Figure 2.5 contains an example where both followers have a value of d_x twice the radius of the circumference described by the leader. As can be seen, the trajectories described by the followers bear no resemblance to the one described by the leader.

In order to gain a greater insight on the concept consider the sketch introduced in figure 2.6. The circumference centred in **L** and with radius d_x contains all the possible solutions for the position of the follower (that is for $d_y = 0$). As seen above there are only two equilibrium points within this set. These two points are the points where the circumference of radius d_x is tangent to the radials of the greater circumference. Choosing an arbitrary value for d_y different from zero results in the possible paths described by the two dashed lines, with radii $r_{a)}$ and $r_{b)}$. From what was seen above, trajectory a) corresponds to a value of θ_d outside the interval $]-\pi/2, \pi/2[$, and thus unstable. On the other hand, solution b), or any other along the line that passes by that point, correspond to a stable solution.

Inspecting figure 2.6 it can be seen that the radius of the circumference described by the follower is given by

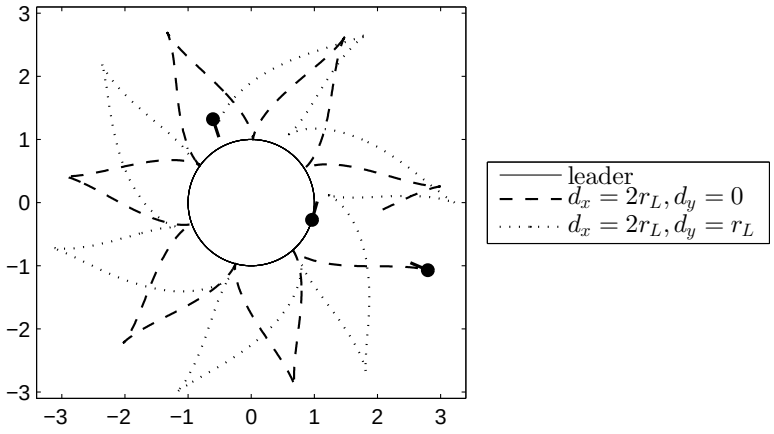

Figure 2.5: Trajectory described by the followers when d_x is two times the radius of the circumference described by the leader, but with different values of d_y.

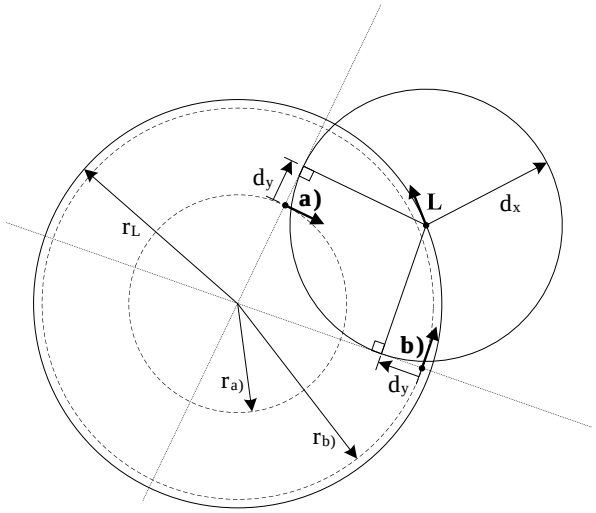

Figure 2.6: Possible follower configurations for a leader tracking a circle.

$$r = \left| \sqrt{r_L^2 - d_x^2} + d_y \right| \tag{2.31}$$

So, for fixed parameters r_L and d_x, the circumference radius can be arbitrarily chosen through d_y. For example, to have a follower describing exactly the same circumference of its leader, one can choose d_y such that $\left| \sqrt{r_L^2 - d_x^2} + d_y \right| = r_L$, or $d_y = \pm r_L - \sqrt{r_L^2 - d_x^2}$. Figure 2.7 shows a configuration where d_x was chosen to be 0.4 of r_L, the radius of leader's circumference, $d_y = \sqrt{r_L^2 - d_x^2} - r_L$ in one case, and $d_y = \sqrt{r_L^2 - d_x^2} + r_L$ in the other, with the later resulting in a follower going backwards. This way, $|\theta_d| < \pi/2$ in both cases, confirming the stability of the equilibrium point (see figure 2.4).

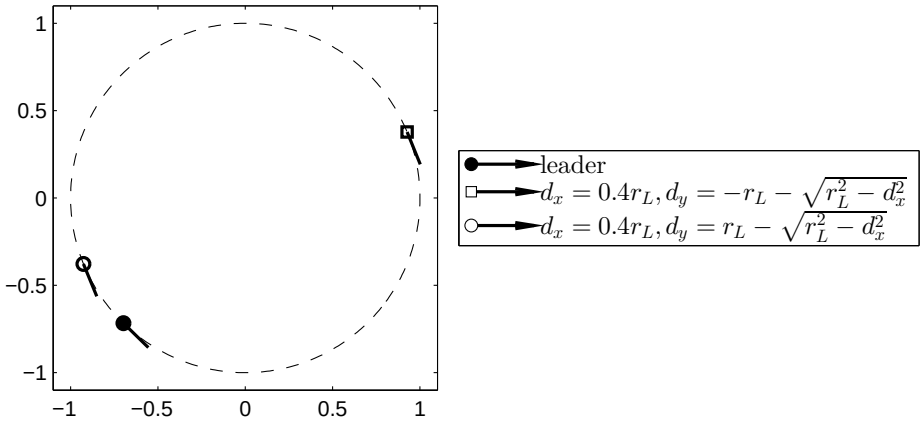

Figure 2.7: Leader and followers describing coincident circles of radius R_0, with the same value of d_x but different d_y.

When $\dot{\kappa}_L \neq 0$ When the trajectory being tracked does not have null κ_L derivative, the analysis is more difficult. In this situation θ_d do not converge to a static value and therefore the Lyapunov analysis made before cannot be applied. Nevertheless, analysing equation (2.29) it is possible to conclude that

- when $d_x\kappa_L \longmapsto 0$, $\dot{\theta}_d \approx -\frac{V_L}{d_x}\sin\theta_d$. In this case, the origin is asymptotically stable and $\theta_d \mapsto 0$. Since $\theta = \theta_d + \theta_L$, θ will approach θ_L, which means that the movement of the follower will be similar to the leader's. An intuitive interpretation to this conclusion is that the follower-leader longitudinal distance (d_x) is very small comparatively to the instantaneous radius of rotation κ_L^{-1}, which imply the angular difference between leader and follower to be close to zero.

- when $d_x\kappa_L \longmapsto \infty$, $\dot{\theta}_d \approx -\omega_L$. In such situation $\theta_d \approx -\theta_L + c$, where c is a constant that depends on the initial conditions. Writing this result in terms of θ, one sees that $\theta \longmapsto c$. This result indicates that, for large values of d_x, θ is slow varying. Intuitively, if the follower is far way from the leader it does not have to move much in order to 'see' the leader in the same position.

This limit analysis indicates that for intermediate values of $d_x\kappa_L$ a trade-off between these two behaviours is to be expected. When the value of $d_x\kappa_L$ is small, the movement of a follower is very similar to the one described by the leader. On the other hand, as $d_x\kappa_L$ grows, the differences between the trajectory described by the leader and the one described by a follower intensify until the motion of the follower starts depending on its initial conditions.

The first sign of divergence is the occurrence of inversions in the direction of movement of a follower. These inversions appear when a follower has to reduce its velocity bellow zero in order to keep accompanying the leader.

Rewriting the first part of equation (2.28) as

$$\frac{u}{V_L} = \cos\theta_d - \frac{d_y}{d_x}\sin\theta_d$$

one sees that the only variables on which the evolution of u depends is V_L and θ_d. In particular, one sees that, for small values of $|\theta_d|$, the following condition for the minimum value of u/V_L can be set

$$\left.\frac{u}{V_L}\right|_{\min} \geq \cos|\theta_d|_{\max} - \left|\frac{d_y}{d_x}\right|\sin|\theta_d|_{\max} \tag{2.32}$$

In order to guarantee that no inversion in the direction of movement of a follower may occur, the condition

$$0 = \cos\theta_d - \frac{d_y}{d_x}\sin\theta_d \Leftrightarrow \tan\theta_d = \frac{d_x}{d_y}$$

can never be verified, which is guaranteed if

$$|\theta_d|_{\max} < \arctan|d_x/d_y| \tag{2.33}$$

From evaluation of equation (2.29) it is possible to extract that

$$|\theta_d|_{\max} = \arcsin\left|d_x\ \kappa_L|_{\theta_d\,\max}\right| \leq \arcsin|d_x\kappa_L|_{\max} \tag{2.34}$$

which gives a bound for θ_d. Having $\arcsin|d_x\kappa_L|_{\max} < \arctan|d_x/d_y|$ guarantees that no inversion in the direction of movement of a follower occurs. Such condition can be used to, given $\mathbf{d}$, set limits on the curvature of the trajectory the leader can describe and vice-versa.

This result is in accordance with what was found for the circumference case. In that case in particular, $\kappa_L = \kappa_{L\,\max} = constant$ and thus $|d_x\kappa_L|_{\max} = 1$ gives the exact limit for the parameters. For other trajectories, however, the bound (2.34) tends to be over-conservative.

In case the trajectory is known, a tighter bound for $|\theta_d|$ can be found by measuring in simulation the maximum value attained for different values of $d_x\kappa_L$ and using these to find an approximated expression.

As an example, consider the application of the above procedure to the determination of a bound for $|\theta_d|_{\max}$ when the leader is describing an '8' trajectory, given by

$$\mathbf{p}_L = \begin{bmatrix} \frac{V_N}{\omega_N}\cos(\omega_N t) \\ \frac{V_N}{2\omega_N}\sin(2\omega_N t) \end{bmatrix} \tag{2.35}$$

where V_N and ω_N are nominal values of linear and angular speeds, respectively.

The curve, which results from the measurement of a total of 100 maximum values, is plotted in figure 2.8 left, against the aforementioned bound and an approximate expression found.

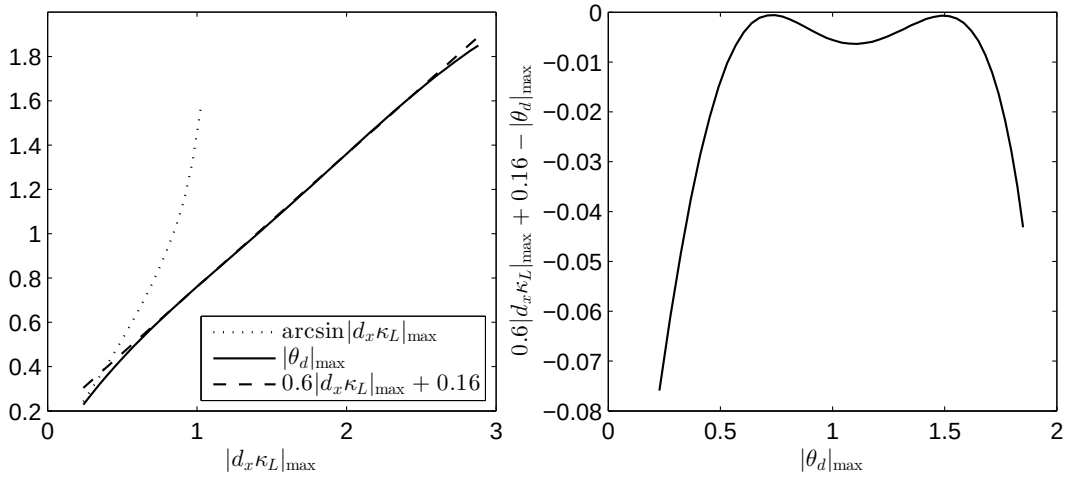

Figure 2.8: Evolution of $|\theta_d|_{\max}$ and of the bound of equation (2.34) with $|d_x\kappa_L|_{\max}$ left (L) and difference between the estimated and effective value of $|\theta_d|_{\max}$ on the right(R).

Comparing the dashed line given by (2.34) and the solid one, in figure 2.8 left, it is clear that, as $|d_x\kappa_L|$ grows, the difference between the bound and the actual value of $|\theta_d|_{\max}$ grows too. When $|d_x\kappa_L| > 1$, equation (2.34) is undefined and cannot be used as a bound for $|\theta_d|_{\max}$, although the actual value is still approximately $\pi/4$.

As can be observed in figure 2.8 left, $|\theta_d|_{\max}$ is approximately proportional to $|d_x\kappa_L|_{\max}$ and is well approximated by the affine line

$$\theta_{d\,\max} = \theta_{d\,\max} = 0.6|d_x\kappa_L|_{\max} + 0.16 \tag{2.36}$$

or, equivalently, noting that $|\kappa_L|_{\max} \approx 4.79\kappa_N$[1], by

$$\theta_{d\,\max} = 2.87 d_x\kappa_N + 0.16 \tag{2.37}$$

Using condition (2.37) together with equation (2.33) it is possible to set the trajectory parameters and the follower configuration in order to guarantee that no inversion occurs. For example, for $\mathbf{d} = [1 \;\; 1]^T$, which imply that $|\theta_d| < \pi/4$, and $V_N = 2$m/s. With this conditions ω_N is limited to

$$\omega_N < \frac{V_N}{d_x}\left(2.87\,\theta_{d\,\max} - 0.16\right) \approx 0.435\,\text{rad/s}$$

whereas, if bound (2.34) were used, the limit for ω_N would be

$$\omega_N < \frac{V_N}{d_x}\frac{\sin\left(\theta_{d\,\max}\right)}{4.79} \approx 0.295\,\text{rad/s}$$

which is more than 30% lower.

[1] For an analysis of the trajectory see appendix A

The same procedure might be applied to any trajectory. However, when the trajectory the leader is assigned is unknown, equations (2.33) and (2.34) should be used.

In some situations it might be of interest to guarantee a minimum speed for the followers. Proceeding in a similar way as in the foregoing case it is possible to set limits on the trajectory parameters and/or on follower configuration to accomplish that objective.

Consider that a minimum follower speed u_m is imposed and, for simplicity, a minimum speed for the leader $V_{L\,\min}$ is set. Choosing

$$\left.\frac{u}{V_L}\right|_{\min} = \frac{u_m}{V_{L\,\min}}$$

and substituting in (2.32) yields

$$\frac{u_m}{V_{L\,\min}} = \cos|\theta_d|_{\max} - \left|\frac{d_y}{d_x}\right| \sin|\theta_d|_{\max} \tag{2.38}$$

At this point it is possible to choose one of two approaches: either set $\mathbf{d}$, solve the above equation for $|\theta_d|_{\max}$ and use the outcome in equation (2.34) to obtain $|\kappa_L|_{\max}$ (for the '8' trajectory, (2.36) may be used alternatively), or choose $|\kappa_L|_{\max}$, use it to obtain $|\theta_d|_{\max}$ and use it in the equation above to set the follower configuration, $\mathbf{d}$. Once one of the ways is taken all the parameters are set.

Since

$$u_{\min} \geq V_{L\,\min} \quad \left.\frac{u}{V_L}\right|_{\min} \tag{2.39}$$

it follows that

$$u_{\min} \geq u_m \tag{2.40}$$

or, put into words, the effective minimum speed $u_{\min}$ is at least equal to, if not greater than, the imposed minimum u_m.

As an example, consider that $u_m = 0.2\mathrm{m/s}$ and $\mathbf{d} = [1\ 1]^T$. Consider also that the leader is to track an '8' trajectory with $V_{L\,\min} = 1\mathrm{m/s}$, which means that $V_N \approx 1.512\mathrm{m/s}$. With this conditions, and using equation (2.37), $\theta_{d\,\max} \approx 0.6435\mathrm{rad}$ and consequently $\kappa_N = 0.1685$. Therefore, the maximum value of ω_N satisfying $u > 0.2\mathrm{m}$ is $\omega_N \approx 0.2547\mathrm{rad/s}$. Using these parameters the minimum speed attained by a follower is $u_{\min} = 0.22\mathrm{m/s}$ which, as imposed, is greater than u_m.

2.5 Results

The developed strategy to control the vehicle described in section 2.2, based on the follow the leader approach proposed in section 2.3, was tested in simulation, using different reference trajectories for the leader.

For all the figures presented in this section the results were generated using $k_1 = 0.3$, $k_2 = 1.5$,

$k_3 = 0$, and $p_{\max} = 5$. Whenever values are introduced without units consider that positions are given in meters $[m]$, velocities in meters per second $[m/s]$, angular speeds in radians per second $[rad/s]$, and angles in radians $[rad]$.

Leader stopped at initial position The following set of figures were generated using $\mathbf{d}_1 = \mathbf{d}_2 = [1\ 1]^T$ and $\mathbf{p}_L = [0\ 0]^T$. In this case the leader stays in the initial position the entire simulation. The initial state of Follower 1 is $\mathbf{p}_{F1}(0) = [-6\ 1]^T$, $u_{F1}(0) = 0.5$, $\omega_{F1}(0) = 0.5$, $\theta_{F1}(0) = -\pi$ and of Follower 2 is $\mathbf{p}_{F2}(0) = [1\ -5]^T$, $u_{F2}(0) = 0$, $\omega_{F2}(0) = 0.5$, $\theta_{F2}(0) = -\pi/2$.

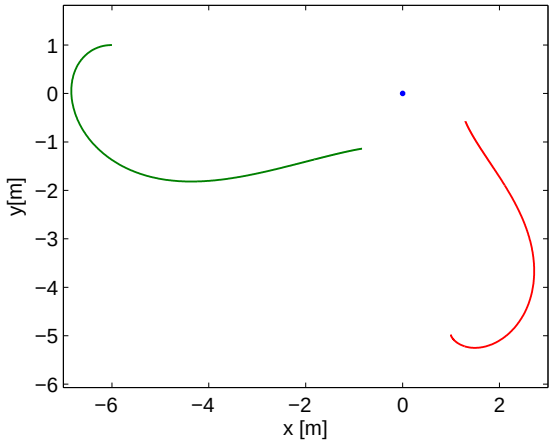

Figure 2.9: Position of leader and followers for the former stopped at $[0\ 0]^T$.

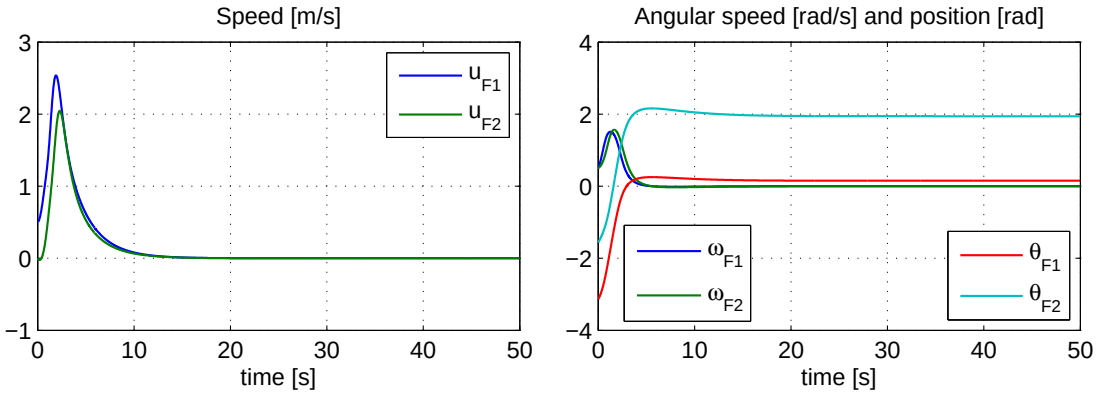

Figure 2.10: Time evolution of forward speed, angular speed and angular position of both followers.

These results confirm that, not only is the origin of the error system asymptotically stable (see figure 2.11), as the Followers converge to stationary positions. Although these positions cannot be determined before hand, being dependent on the initial conditions of the followers, as can be concluded from figure 2.9, given an angular position θ there is only one possible position for a follower, and vice-versa.

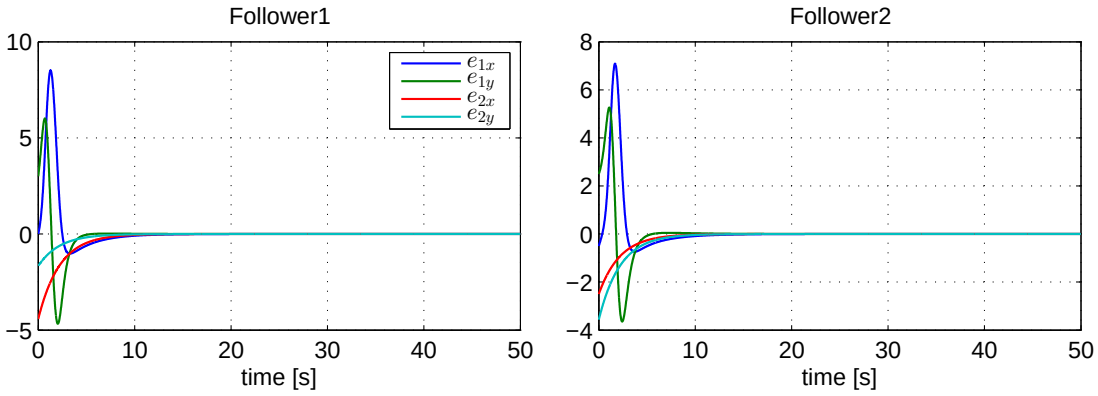

Figure 2.11: Time evolution of the components of errors $\mathbf{e}_1$ and $\mathbf{e}_2$ of both followers.

Leader describing an '8' The following set of figures were generated using $\mathbf{d}_1 = [0.35\ 0.35]^T$, $\mathbf{d}_2 = [0.35\ -0.35]^T$ and $\mathbf{p}_L = [2\cos(0.25t)\ \sin(0.5t)]^T$. The initial state of Follower 1 is $\mathbf{p}_{F1}(0) = [3\ 3]^T$, $u_{F1}(0) = 0.5$, $\omega_{F1}(0) = 0.5$, $\theta_{F1}(0) = 3\pi/2$ and of Follower 2 is $\mathbf{p}_{F2}(0) = [3\ 1]^T$, $u_{F2}(0) = 0$, $\omega_{F2}(0) = 0.5$, $\theta_{F2}(0) = 0$.

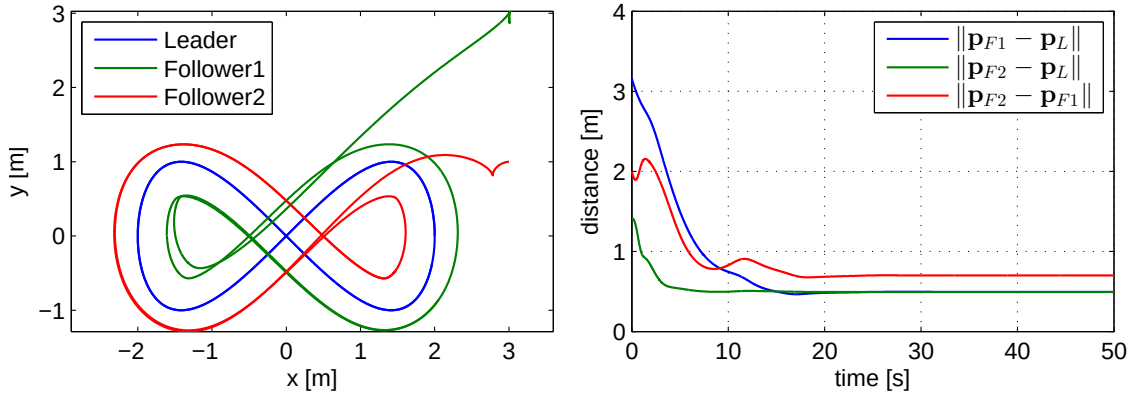

Figure 2.12: Position of the leader and followers for the former describing an '8' with $\omega_N = 0.25\text{rad/s}$ and $V_N = 0.5\text{m/s}$.

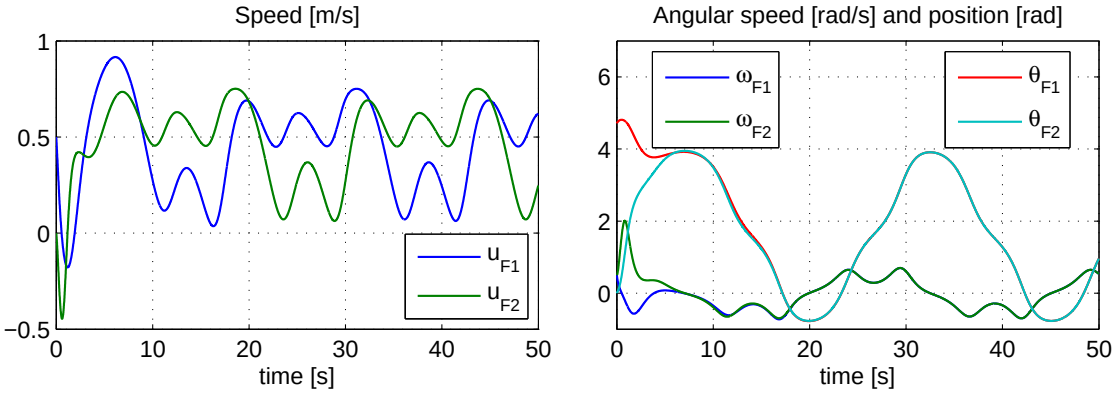

Figure 2.13: Time evolution of forward speed, angular speed and angular position of both the followers.

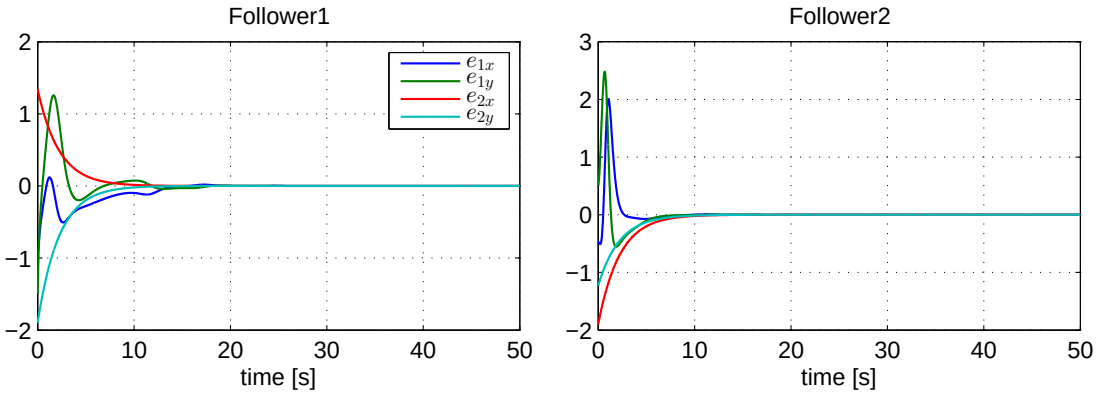

Figure 2.14: Time evolution of the components of the errors $\mathbf{e}_1$ and $\mathbf{e}_2$ of both the followers.

The trajectory described by each Follower at the beginning of the simulation is quite unpredictable (see figure 2.12 left) and behaviours such as inversions in the direction of movement are likely to happen.

Although the trajectories of both followers are different (figure 2.12), their angular speed and position, converge to one another, as can be concluded from observation of figure 2.13 right. This is in accordance with the analysis made in section 2.4, where it was concluded that these variables do not depend on d_y, the only parameter that is different between followers in this simulation.

Lastly, figure 2.12 right indicates that the distance between followers and between these and the leader converge to fixed values. The later is a direct implication of the asymptotic stability of the error system. The former, the distance between followers, is a result of the independence of each follower's u, ω and θ from d_y. The limit to which this distance converges is equal to the sum of the followers distance, in this case $0.35 + 0.35 = 0.7\mathrm{m}$. These results indicate that, a formation where all the followers have the same value of d_x is asymptotically a rigid formation.

2.6 Trajectory planner

2.6.1 Concept

The concept of leader-following developed for virtual vehicles can be exploited to control formations of any type of vehicle. The idea consists in using the trajectories described by the virtual vehicles as reference trajectories for real vehicles. The virtual followers are grouped in one entity called trajectory planner that generates trajectories for the followers (real vehicles) based on the motion of another real vehicle, the leader. The concept is illustrated in figure 2.15.

Contrary to a strategy developed specifically to a certain type of vehicle, this approach can be used to coordinate the motion of any type of vehicles, given that they are equipped with trajectory tracking controllers.

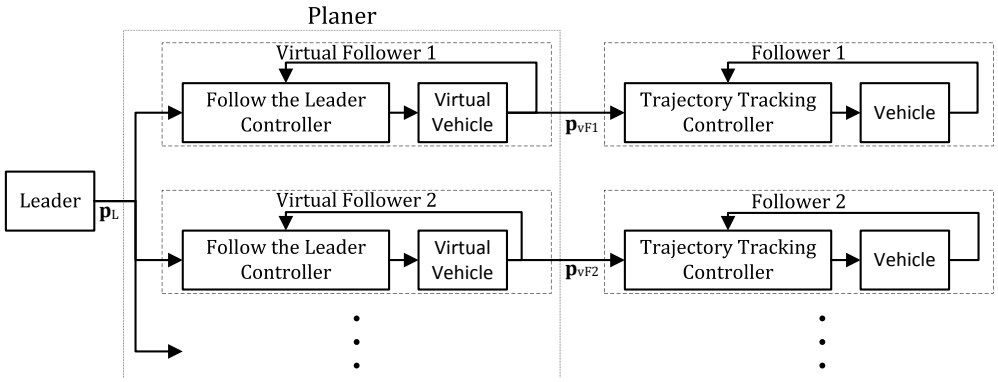

Figure 2.15: Block diagram showing the leader-following strategy applied.

2.6.2 Three-dimensional trajectories

In order to use the derived laws, which live in a two-dimensional space, to generate three-dimensional trajectories it is necessary to extend the state to include the vertical motion. Instead of deriving a law for the entire state space, a separated control law is designed to drive the vertical coordinate of the virtual follower to a desired distance to the leader. Consider that the desired vectorial distance $\mathbf{d}$ is now extended to include a third component d_z. The objective of this simple law is to drive the third component of the generated trajectory p_{Fz} to $p_{Lz} - d_z$, $\dot{p}_{Fz}$ to $\dot{p}_{Lz}$ and $\ddot{p}_{Fz}$ to $\ddot{p}_{Lz}$.

Let e_z be the vertical position error given by

$$e_z = p_{Lz} - p_{Fz} - d_z \tag{2.41}$$

A control law for e_z might be given by

$$\ddot{p}_{Fz} = \sigma_z \left(\ddot{p}_{Lz} + k_{z1} e_z + k_{z2} \dot{e}_z \right) \tag{2.42}$$

Where, $\sigma_z(x)$ is a saturation function given by

$$\sigma_z(x) = \begin{cases} x & \text{if } |x| < z_{\max} \\ \text{sign}(x) z_{\max} & \text{if } |x| > z_{\max} \end{cases} \tag{2.43}$$

The parameter $z_{\max}$ can be adjusted depending on the type of vehicle intended to track the trajectory. This saturation is introduced to protect the followers from any unexpected acceleration of the leader. The control law guarantees asymptotic stability of e_z if the condition $\ddot{\mathbf{p}}_{Lz} < z_{\max}$ is verified.

2.6.3 Formation initialisation

Recalling the figures presented in last section, it has been observed that during the formation initialization inversions in the direction of movement of the virtual followers are likely to occur (see figure 2.12). Whilst this behaviour is normal and expectable for a non-holonomic car it is undesirable for a following vehicle that is tracking the described trajectory.

To prevent such from happening the virtual followers are started at their intended initial positions. Using information from the reference trajectory of the leader, the virtual followers are placed initially with null errors with respect to the reference trajectory, and oriented in the initial planar direction of the reference trajectory, i.e. the normalised projection of the reference velocity at $t = 0$.

Let $\theta_{ref}(0)$ be the initial reference direction, given by

$$\theta_{ref}(0) = \arctan\left(\frac{\mathbf{j}^T\dot{\mathbf{p}}_{ref}(0)}{\mathbf{i}^T\dot{\mathbf{p}}_{ref}(0)}\right)$$

the position at which each virtual follower is initially placed is simply given by

$$\mathbf{p}_{vFi}(0) = \mathbf{p}_{ref}(0) - \begin{bmatrix} \cos\theta_{ref}(0) & -\sin\theta_{ref}(0) & 0 \\ \sin\theta_{ref}(0) & \cos\theta_{ref}(0) & 0 \\ 0 & 0 & 1 \end{bmatrix} \mathbf{d}_i \tag{2.44}$$

where the subscript i is relative to the virtual follower considered.

Until both leader and following vehicles approach the initial reference and virtual followers, respectively, the controllers of the virtual vehicles are turned off. Once that happens these controllers are turned on and the leader starts tracking the reference trajectory.

The start of the tracking is triggered when the positional errors of each vehicle enter a set $e_i = \|\mathbf{p}_{Fi} - \mathbf{p}_{vFi}(0)\| < e_{\max}$.

$$trigger = (e_L < e_{\max}) \wedge e_1 < e_{\max}) \wedge (e_2 < e_{\max}) \wedge \cdots \wedge (e_n < e_{\max}) \tag{2.45}$$

where $e_{\max}$ is a configurable parameter to adjust the minimum error to start the tracking.

Note that this approach to initialise the formation only requires the initial reference to be provided to the planner. Once the formation is moving only the leader's trajectory is passed.

2.7 Summary

This chapter presented the trajectory planner developed to control formations of autonomous vehicles. It is composed of a group of virtual vehicles modelled as nonholonomic cars that are controlled using a law described in this chapter. Formal proof of global asymptotic stability of the

origin of the error system was provided and the stability of the inner dynamics analysed. Although it could not be demonstrated, a limit analysis showed that the evolution of the state variables is bounded. If some limits on the curvature of the trajectory described by the leader and on the desired distance of each follower are respected, the movement of the followers is deterministic and very similar to the movement of the leader.

During formation initialisation it has been observed the occurrence of inversions in the directions of movement of the virtual followers. To prevent this behaviour from affecting the movement of the followers, the virtual followers are initially positioned with null errors and the planner is only started when the formation is established.

In order to use the virtual followers to generate three-dimensional trajectories it was necessary to introduce a control law for the vertical direction. This law limits the vertical acceleration of the generated trajectory in order to protect the following vehicles from any extreme acceleration of the leader. Grouping the vertical law with the equations that govern the motion on the horizontal plane results in the following set

$$\begin{aligned}
\ddot{\mathbf{p}}_F &= \begin{bmatrix} \mathcal{R}\mathbf{S}(\omega)\mathbf{i}u + \mathcal{R}\mathbf{i}T \\ \sigma_z \left(\ddot{p}_{Lz} + k_{z1}e_z + k_{z2}\dot{e}_z\right) \end{bmatrix} \\
\dot{\mathcal{R}} &= \mathcal{R}\mathbf{S}(\omega) \\
\dot{u} &= T \\
\dot{\omega} &= \tau \\
\begin{bmatrix} T \\ \tau \end{bmatrix} &= \Gamma^{-1}\left(\boldsymbol{\delta} + k_1\dot{\boldsymbol{\sigma}}(\mathbf{e_1}) + k_1^2 k_2 \mathbf{e}_2\right)
\end{aligned} \tag{2.46}$$

Chapter 3

Quadrotors in formation

In the present chapter, the performance of the trajectory planner in controlling a formation of quadrotor vehicles is assessed in simulation. Towards that end, a quadrotor model and a trajectory tracking controller are presented in sections 3.1 and 3.2, respectively. Section 3.3 presents the results of simulations conducted to test the quadrotor controller, firstly, and the coordinated flight using the developed planner.

3.1 Quadrotor Model

3.1.1 Kinematics

The description of the quadrotor model requires the definition of two coordinate frames: the inertial frame $\{I\}$ and the body frame $\{B\}$.

The inertial frame The frame $\{I\}$ is an orthogonal frame defined by the canonical basis $\{\mathbf{i}, \mathbf{j}, \mathbf{k}\}$ with $\mathbf{i}$ oriented northward, $\mathbf{j}$ eastward and $\mathbf{k}$ pointing to Nadir. In the literature, this frame is usually referred to as the NED frame (North-East-Down). It is assumed that the Earth is flat and still.

The body frame The frame $\{B\}$ is defined by the set of unitary vectors $\{\mathbf{i}_B, \mathbf{j}_B, \mathbf{k}_B\}$ with $\mathbf{k}_B$ aligned with the vehicle's thrust vector, but oriented in the opposite direction, and $\mathbf{j}_B$ and $\mathbf{i}_B$ aligned in order to form an orthogonal set. The origin of this frame is in the body's centre of mass.

Mapping between frames The correspondence between body and inertial frames is defined in a similar way as it was in the 2-D model. The difference is the extension of dimensions and thus,

the rotation matrix is now given by:

$$ {}^{I}_{B}\mathbf{R} = \begin{bmatrix} \mathbf{i}\cdot\mathbf{i}_B & \mathbf{i}\cdot\mathbf{j}_B & \mathbf{i}\cdot\mathbf{k}_B \\ \mathbf{j}\cdot\mathbf{i}_B & \mathbf{j}\cdot\mathbf{j}_B & \mathbf{j}\cdot\mathbf{k}_B \\ \mathbf{k}\cdot\mathbf{i}_B & \mathbf{k}\cdot\mathbf{j}_B & \mathbf{k}\cdot\mathbf{k}_B \end{bmatrix} \tag{3.1} $$

As in the two-dimensional case, it is possible to parametrise a rotation matrix through a set of angles representing the angular displacements between the two frames, these are called Euler angles. Since there are three angular degrees of freedom, it is necessary to define three angles, each representing a rotation around one axis. Depending on the sequence of rotations different angles are obtained. In aircrafts and helicopters the sequence 'ZYX' (meaning that the first rotation is performed around $\mathbf{k}$ and so forth) is usually used, associated with the angles ψ (yaw), θ (pitch) and ϕ (roll), respectively. A rotation matrix as a function of the angles $\{\psi, \theta, \phi\}$ is given by

$$ \mathbf{R} = \begin{bmatrix} \cos\psi\cos\theta & \cos\psi\sin\theta\sin\phi - \sin\psi\cos\phi & \cos\psi\sin\theta\cos\phi + \sin\psi\sin\phi \\ \sin\psi\cos\theta & \sin\psi\sin\theta\sin\phi + \cos\psi\cos\phi & \sin\psi\sin\theta\cos\phi - \cos\psi\sin\phi \\ -\sin\theta & \cos\theta\sin\phi & \cos\theta\cos\phi \end{bmatrix} \tag{3.2} $$

The problem of this parametrisation is the existence of singularities when $\theta = \pm\pi/2$. Other parametrisations such as quaternions or angle-axis could be used, but these also present some drawbacks. Thus, the control law presented in next section is derived using matrices of rotation, although Euler angles are used in this thesis to present data as they are more intuitive to understand.

Going back to equation (3.1) and computing its time derivative it yields

$$ {}^{I}_{B}\dot{\mathbf{R}} = \mathbf{S}({}^{I}\boldsymbol{\omega}_B){}^{I}_{B}\mathbf{R} = {}^{I}_{B}\mathbf{R}\mathbf{S}\left({}^{B}({}^{I}\boldsymbol{\omega}_B)\right) \tag{3.3} $$

where $\mathbf{S}(\mathbf{x}) \in \mathbb{R}^{3\times3}$ is the cross product matrix $\mathbf{S}(\mathbf{x})\mathbf{y} = \mathbf{x}\times\mathbf{y}$.

The other kinematic equation is defined as in

$$ {}^{I}\dot{\mathbf{p}}_B = {}^{I}_{B}\mathbf{R}\,{}^{B}({}^{I}\mathbf{v}_B) \tag{3.4} $$

For the purpose of simplification of notation, the following definitions are used

$$ \mathcal{R} = \begin{bmatrix} \mathbf{r}_1 & \mathbf{r}_2 & \mathbf{r}_3 \end{bmatrix} = {}^{I}_{B}\mathbf{R} \tag{3.5} $$

$$ \mathbf{v} = {}^{B}({}^{I}\mathbf{v}_B) \tag{3.6} $$

$$ \boldsymbol{\omega} = {}^{B}({}^{I}\boldsymbol{\omega}_B) \tag{3.7} $$

$$ \mathbf{p} = {}^{I}\mathbf{p}_B \tag{3.8} $$

3.1.2 Dynamics

From *Newton*'s second law, a change in linear momentum equals the sum of all the external forces acting on the body. In a similar way, a change in angular momentum equals the sum of all the external moments applied.

$$\sum_{i}^{N} {}^{I}\mathbf{f}_i = {}^{I}\mathbf{f} = \frac{d}{dt}\left(m\mathcal{R}\mathbf{v}\right) = m\left(\mathcal{R}\mathbf{S}(\boldsymbol{\omega})\mathbf{v} + \mathcal{R}\dot{\mathbf{v}}\right)$$
$$\sum_{i}^{N} {}^{I}\mathbf{n}_i = {}^{I}\mathbf{n} = \dot{\mathcal{R}}\mathbf{J}\boldsymbol{\omega} + \mathcal{R}\mathbf{J}\dot{\boldsymbol{\omega}} = \mathcal{R}\mathbf{S}(\boldsymbol{\omega})\mathbf{J}\boldsymbol{\omega} + \mathcal{R}\mathbf{J}\dot{\boldsymbol{\omega}}$$

The matrix $\mathbf{J} \in \mathbb{R}^3$ represents the quadrotor tensor of inertia. Given the symmetries of the quadrotor body, the products of inertia are assumed zero. Hence, the tensor of inertia reduces to a diagonal matrix with elements J_{xx}, J_{yy} and J_{zz}.

The above equations are usually represented in the body frame and in the standard format of differential equations.

$$\dot{\mathbf{v}} = -\mathbf{S}(\boldsymbol{\omega})\mathbf{v} + \frac{1}{m}\mathcal{R}^{T}\,{}^{I}\mathbf{f} = -\mathbf{S}(\boldsymbol{\omega})\mathbf{v} + \frac{1}{m}\mathbf{f} \tag{3.9}$$
$$\dot{\boldsymbol{\omega}} = -\mathbf{J}^{-1}\mathbf{S}(\boldsymbol{\omega})\mathbf{J}\boldsymbol{\omega} + \mathbf{J}^{-1}\mathcal{R}^{T}\,{}^{I}\mathbf{n} = -\mathbf{J}^{-1}\mathbf{S}(\boldsymbol{\omega})\mathbf{J}\boldsymbol{\omega} + \mathbf{J}^{-1}\mathbf{n} \tag{3.10}$$

Proceeding building a model for the quadrotor, consider figure 3.1. The forces acting on the body are the rotors' thrust T_i, with $i = \{1, 2, 3, 4\}$, aligned with $\mathbf{k}_B$ and the gravity acceleration aligned with the inertial frame's down axis $\mathbf{k}$. Transforming the forces to the body frame and substituting in equation 3.9 yields

$$\dot{\mathbf{v}} = -\mathbf{S}(\boldsymbol{\omega})\mathbf{v} + g\mathcal{R}^{T}\mathbf{k} - \frac{1}{m}\sum_{i=1}^{4} T_i\mathbf{k} \tag{3.11}$$

The moments applied to the quadrotor result from the forces that are not collinear with the centre of mass and from the torques originated in the rotors. Each of the rotors produce a permanent torque to counteract the drag on the blades and friction generated inside the motor. The torques Q_i are aligned with the axis Oz and their sign depend on the rotation (either positive or negative).

Grouping the contributions of each rotor, the resultant moment is

$$\mathbf{n} = -\sum_{i=1}^{4}\left(\mathbf{r}_{pi} \times T_i\mathbf{k} + (-1)^{i}Q_i\mathbf{k}\right) \tag{3.12}$$

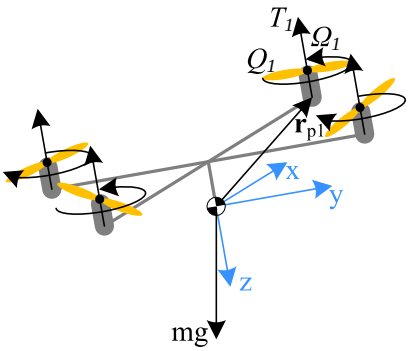

$\mathbf{r}_{p\{1,3\}} = \begin{bmatrix} \pm b & 0 & -h \end{bmatrix}^T$
$\mathbf{r}_{p\{2,4\}} = \begin{bmatrix} 0 & \pm b & -h \end{bmatrix}^T$
$\Omega_i \equiv$ rotor i angular speed

Figure 3.1: Diagram of a quadrotor and forces applied.

3.1.3 Aerodynamics

The thrust T_i and torque Q_i can be written as functions of each rotor's angular speed [29], [30].

$$\begin{aligned} T_i &= \rho A \Omega_i^2 R^2 C_T \\ Q_i &= \rho A \Omega_i^2 R^3 C_Q \end{aligned} \tag{3.13}$$

where Ω_i is the angular speed of the rotor, R is the rotor disk radius, C_T the coefficient of thrust and C_Q the coefficient of torque. In the generality of applications, quadrotor models consider that C_T and C_Q are constant parameters (see for example [31] and [32]). At low air speeds, typically under *Mach* numbers of 0.3, the effects of compressibility can be neglected [33], so ρ (air density) may be assumed constant. Since the objective of this thesis is not to produce a very exhaustive model of the quadrotor these approximations are used.

When such simplifications are considered the equations of thrust and torque can be rewritten in the form

$$T_i = k_T \Omega_i^2 \qquad\qquad Q_i = k_Q \Omega_i^2$$

and the resulting moments and forces can be written in a compact form

$$\begin{bmatrix} T \\ \mathbf{n} \end{bmatrix} = \begin{bmatrix} k_T & k_T & k_T & k_T \\ 0 & -bk_T & 0 & bk_T \\ bk_T & 0 & -bk_T & 0 \\ k_Q & -k_Q & k_Q & -k_Q \end{bmatrix} \begin{bmatrix} \Omega_1^2 \\ \Omega_2^2 \\ \Omega_3^2 \\ \Omega_4^2 \end{bmatrix} \tag{3.14}$$

which gives a direct relation between rotors' angular speeds and thrust and torque. In the foregoing analysis contributions resulting from delayed motors' response, variation of the angular momentum of the rotors and contributions resulting from blade flapping were neglected. For a deeper analysis concerning these topics see for instance [29], [34], or [35]. This approach to modelling the rotors has the advantage of reducing the identification process to the determination of two constants, k_T and k_Q.

For simplicity, and since their relation to rotors' angular speed is direct, T and $\mathbf{n}$ will be used as control inputs. The same approach is used in [32] and [36], for example. Using the input transformation

$$\boldsymbol{\tau} = \mathbf{J}^{-1}\mathbf{S}(\boldsymbol{\omega})\mathbf{J}\boldsymbol{\omega} + \mathbf{J}^{-1}\mathbf{n} \tag{3.15}$$

equation (3.10) reduces to the integrator form $\dot{\boldsymbol{\omega}} = \boldsymbol{\tau}$. With this simplification, the model description is finally concluded.

3.1.4 Model Summary

The quadrotor model described can be summarised with the following set of equations:

$$\begin{aligned}
\dot{\mathbf{p}} &= \mathcal{R}\mathbf{v} \\
\dot{\mathcal{R}} &= \mathcal{R}\mathbf{S}(\boldsymbol{\omega}) \\
\dot{\mathbf{v}} &= -\mathbf{S}(\boldsymbol{\omega})\mathbf{v} + g\mathcal{R}^T\mathbf{k} - \frac{1}{m}T\mathbf{k} \\
\dot{\boldsymbol{\omega}} &= -\mathbf{J}^{-1}\mathbf{S}(\boldsymbol{\omega})\mathbf{J}\boldsymbol{\omega} + \mathbf{J}^{-1}\mathbf{n} = \boldsymbol{\tau}
\end{aligned} \tag{3.16}$$

3.2 Quadrotor Trajectory Tracking Controller

Using the quadrotor model derived a trajectory tracking control law is designed starting from the main objective and creating errors and expanding the Lyapunov candidate until uncovering the control inputs. Towards that end, consider the first objective which is to drive the quadrotor's position to a desired position given by $\mathbf{p}_d$, and the associated error $\mathbf{e}_1$.

$$\begin{aligned}
\mathbf{e}_1 &= \mathbf{p} - \mathbf{p}_d \\
\dot{\mathbf{e}}_1 &= \mathcal{R}\mathbf{v} - \dot{\mathbf{p}}_d
\end{aligned} \tag{3.17}$$

Instead of proceeding with the natural backstepping procedure, a new error $\mathbf{e}_2$ is created to equal $\dot{\mathbf{e}}_1$.

$$\mathbf{e}_2 = \dot{\mathbf{e}}_1 \tag{3.18}$$

$$\begin{aligned}\dot{\mathbf{e}}_2 =&\ddot{\mathbf{e}}_1 = \frac{1}{m}\mathcal{R}\mathbf{f} - \ddot{\mathbf{p}}_d = -\frac{T}{m}\mathcal{R}\mathbf{k} + g\mathbf{k} - \ddot{\mathbf{p}}_d \\ =& -\boldsymbol{\sigma}_e\left(k_1\mathbf{e}_1 + k_2\mathbf{e}_2\right) + \left(-\frac{T}{m}\mathcal{R}\mathbf{k} + g\mathbf{k} - \ddot{\mathbf{p}}_d + \boldsymbol{\sigma}_e\left(k_1\mathbf{e}_1 + k_2\mathbf{e}_2\right)\right)\end{aligned}$$

where $\boldsymbol{\sigma}_e(\mathbf{x})$ is an element wise saturation function given by

$$\boldsymbol{\sigma}_e(\mathbf{x}) = \sigma_{\max}\frac{x_i}{\sqrt{c + x_i^2}} \tag{3.19}$$

which is introduced to limit the influence of errors $\mathbf{e}_1$ and $\mathbf{e}_2$ in the subsequent steps of backstepping. The dependency of $\boldsymbol{\sigma}_e$ on $k_1\mathbf{e}_1 + k_2\mathbf{e}_2$ will be omitted in most of the coming description for greater compactness.

Let T_d and $\mathbf{r}_{3d}$ be the desired thrust and thrust direction, respectively, and let them be given by

$$T_d = m\|g\mathbf{k} - \ddot{\mathbf{p}}_d + \boldsymbol{\sigma}_e\| \tag{3.20}$$

$$\mathbf{r}_{3d} = \frac{g\mathbf{k} - \ddot{\mathbf{p}}_d + \boldsymbol{\sigma}_e}{\|g\mathbf{k} - \ddot{\mathbf{p}}_d + \boldsymbol{\sigma}_e\|} \tag{3.21}$$

The desired thrust direction is not well defined for $T_d = 0$. To guarantee that such never happens the limits of $\boldsymbol{\sigma}_e$ must be chosen carefully. Concentrating on the third component of $\mathbf{r}_{3d}$ and recalling that, by equation (2.43), $|\mathbf{k}^T\ddot{\mathbf{p}}_d|$ is limited to $z_{\max}$, it is possible to set an upper limit to $\sigma_{\max}$ given by

$$\sigma_{\max} < g - z_{\max} \tag{3.22}$$

Using this saturation, $T_d = 0$ can never be verified.

A control law for the thrust is now defined using these two quantities

$$T = \mathbf{r}_{3d}^T\mathbf{r}_3 T_d \tag{3.23}$$

Substitution of (3.23) into $\dot{\mathbf{e}}_2$ allows it to be rewritten as

$$\begin{aligned}\dot{\mathbf{e}}_2 =& -\boldsymbol{\sigma}_e + \frac{1}{m}\left(T_d\mathbf{r}_{3d} - T\mathbf{r}_3\right) \\ =& -\boldsymbol{\sigma}_e - \frac{T_d}{m}\mathbf{S}(\mathbf{r_3})^2\mathbf{r}_{3d}\end{aligned}$$

Consider a Lyapunov candidate function V_σ given by

$$V_\sigma = \frac{1}{2}\begin{bmatrix}\boldsymbol{\sigma}_e^T & \mathbf{e}_2^T\end{bmatrix}\mathbf{P}\begin{bmatrix}\boldsymbol{\sigma}_e \\ \mathbf{e}_2\end{bmatrix} + \sum_{i=x,y,z}\int_0^{k_1e_{1i}+k_2e_{2i}}\sigma_e(u)du \tag{3.24}$$

where $\mathbf{P}$ is a constant, symmetric and positive definite matrix given by

$$\mathbf{P} = \begin{bmatrix} p_{11}\mathbf{I}_3 & -p_{12}\mathbf{I}_3 \\ -p_{12}\mathbf{I}_3 & p_{22}\mathbf{I}_3 \end{bmatrix} \tag{3.25}$$

with $p_{11}, p_{22} > 0$ and $p_{12}^2 < p_{11}p_{22}$. The first term of (3.24) is quadratic and thus positive. The second term is the integral of a monotonically increasing function, which is positive too. Therefore (3.24) is a positive function. Computing the time derivative of V yields

$$\begin{aligned} \dot{V}_\sigma &= \begin{bmatrix} \boldsymbol{\sigma}_e^T & \mathbf{e}_2^T \end{bmatrix} \mathbf{P} \begin{bmatrix} \dot{\boldsymbol{\sigma}}_e \\ \dot{\mathbf{e}}_2 \end{bmatrix} + \boldsymbol{\sigma}_e^T \cdot (k_1\dot{\mathbf{e}}_1 + k_2\dot{\mathbf{e}}_2) \\ &= \begin{bmatrix} \boldsymbol{\sigma}_e^T & \mathbf{e}_2^T \end{bmatrix} \mathbf{P} \begin{bmatrix} \boldsymbol{\sigma}_e' \cdot (k_1\dot{\mathbf{e}}_1 + k_2\dot{\mathbf{e}}_2) \\ -\boldsymbol{\sigma}_e - \dfrac{T_d}{m}\mathbf{S}(\mathbf{r_3})^2\mathbf{r}_{3d} \end{bmatrix} + \boldsymbol{\sigma}_e \cdot \left[k_1\mathbf{e}_2 - k_2\left(\boldsymbol{\sigma}_e + \frac{T_d}{m}\mathbf{S}(\mathbf{r_3})^2\mathbf{r}_{3d} \right) \right] \end{aligned}$$

The apostrophe on $\boldsymbol{\sigma}_e'$ denotes the partial derivative of $\boldsymbol{\sigma}_e$ with respect to its argument, $\frac{\partial}{\partial \mathbf{x}}\boldsymbol{\sigma}_e(\mathbf{x})$, which is a diagonal matrix. Some mathematical manipulation allows $\dot{V}_\sigma$ do be rewritten in the form

$$\dot{V}_\sigma = -\begin{bmatrix} \boldsymbol{\sigma}_e^T & \mathbf{e}_2^T \end{bmatrix} \mathbf{Q} \begin{bmatrix} \boldsymbol{\sigma}_e \\ \mathbf{e}_2 \end{bmatrix} - \left[k_2\left(p_{11}\boldsymbol{\sigma}_e^T - p_{12}\mathbf{e}_2^T \right)\boldsymbol{\sigma}_e' + (k_2 - p_{12})\,\boldsymbol{\sigma}_e^T + p_{22}\mathbf{e}_2^T \right] \frac{T_d}{m}\mathbf{S}(\mathbf{r_3})^2\mathbf{r}_{3d} \tag{3.26}$$

The matrix $\mathbf{Q}$ is given by

$$\mathbf{Q} = \begin{bmatrix} (k_2 - p_{12})\mathbf{I}_3 + p_{11}k_2\boldsymbol{\sigma}_e' & -\dfrac{k_1p_{11} + k_2p_{12}}{2}\boldsymbol{\sigma}_e' - \dfrac{k_1 - p_{22}}{2}\mathbf{I}_3 \\ -\dfrac{k_1p_{11} + k_2p_{12}}{2}\boldsymbol{\sigma}_e' - \dfrac{k_1 - p_{22}}{2}\mathbf{I}_3 & p_{12}k_1\boldsymbol{\sigma}_e' \end{bmatrix} \tag{3.27}$$

With a proper choice of gains and coefficients of $\mathbf{P}$, $\mathbf{Q}$ can be made positive definite. Choosing $k_1 = p_{22}$ and $k_2 = p_{11}p_{22}/p_{12}$, $\mathbf{Q}$ becomes

$$\mathbf{Q} = \begin{bmatrix} \dfrac{1}{p_{12}}\left[(p_{11}p_{22} - p_{12}^2)\mathbf{I}_3 + p_{11}^2p_{22}\boldsymbol{\sigma}_e' \right] & -p_{22}p_{11}\boldsymbol{\sigma}_e' \\ -p_{22}p_{11}\boldsymbol{\sigma}_e' & p_{12}p_{22}\boldsymbol{\sigma}_e' \end{bmatrix} \tag{3.28}$$

Since $\mathbf{Q}$ is a block matrix, its determinant is given by (see [37])

$$\begin{aligned} \det(\mathbf{Q}) &= \det(\mathbf{Q}_{22}) \cdot \det(\mathbf{Q}_{11} - \mathbf{Q}_{12}\mathbf{Q}_{22}^{-1}\mathbf{Q}_{21}) \\ &= \det(p_{12}p_{22}\boldsymbol{\sigma}_e') \cdot \det\left(\frac{p_{11}p_{22} - p_{12}^2}{p_{12}}\mathbf{I}_3 \right) \\ &= p_{22}(p_{11}p_{22} - p_{12}^2)\det(\boldsymbol{\sigma}_e') \end{aligned}$$

Since $\boldsymbol{\sigma}_e$ is a diagonal matrix with positive elements, its determinant is positive. From the imposition of positive definiteness of $\mathbf{P}$ it follows that $p_{22} > 0$ and $p_{12}^2 < p_{11}p_{22}$. Therefore $\mathbf{Q}$ is positive

definite.

For a more compact writing consider the introduction of a new variable $\boldsymbol{\delta}$ given by

$$\boldsymbol{\delta}\left(\mathbf{e}_1, \mathbf{e}_2\right) = k_2 p_{12} \boldsymbol{\sigma}_e' \left(\frac{k_2}{k_1}\boldsymbol{\sigma}_e - \mathbf{e}_2\right) + \left(k_2 - p_{12}\right)\boldsymbol{\sigma}_e + k_1 \mathbf{e}_2 \tag{3.29}$$

and a positive function $W(\mathbf{e}_1, \mathbf{e}_2)$ given by

$$W_\sigma(\mathbf{e}_1, \mathbf{e}_2) = \begin{bmatrix}\boldsymbol{\sigma}_e^T & \mathbf{e}_2^T\end{bmatrix} \mathbf{Q} \begin{bmatrix}\boldsymbol{\sigma}_e \\ \mathbf{e}_2\end{bmatrix} \tag{3.30}$$

Using these two definitions, (3.26) becomes

$$\dot{V}_\sigma = -W_\sigma(\mathbf{e}_1, \mathbf{e}_2) - \frac{T_d}{m}\mathbf{r}_{3d}^T \mathbf{S}(\mathbf{r_3})^2 \boldsymbol{\delta}\left(\mathbf{e}_1, \mathbf{e}_2\right) \tag{3.31}$$

The first term of the equation(3.31) is negative definite, whereas the second term is indefinite. To drive the second term to zero a new error is created and the candidate Lyapunov extended to include it.

$$\mathbf{e}_3 = \mathbf{r}_3 - \mathbf{r}_{3d} \tag{3.32}$$

$$V_3 = V_\sigma + \frac{1}{2}\mathbf{e}_3^T \mathbf{e}_3 \tag{3.33}$$

Computing the time derivative of V_3 yields

$$\begin{aligned}
\dot{V}_3 =& \dot{V}_\sigma - \mathbf{r}_{3d}^T \dot{\mathbf{r}}_3 - \mathbf{r}_3^T \dot{\mathbf{r}}_{3d} \\
=& \dot{V}_\sigma + \mathbf{r}_{3d}^T \mathcal{R}\mathbf{S}(\mathbf{k})\left(\boldsymbol{\omega} - \mathcal{R}^T \mathbf{S}\left(\mathbf{r}_{3d}\right)\dot{\mathbf{r}}_{3d}\right) \\
=& -W_\sigma(\mathbf{e}_1, \mathbf{e}_2) - k_3 \mathbf{r}_{3d}^T \mathbf{S}(\mathbf{r}_3)^T \mathbf{S}(\mathbf{r}_3)\mathbf{r}_{3d} \\
& + \mathbf{r}_{3d}^T \mathcal{R}\mathbf{S}(\mathbf{k})\left(\boldsymbol{\omega} - \mathcal{R}^T \mathbf{S}\left(\mathbf{r}_{3d}\right)\dot{\mathbf{r}}_{3d} - k_3 \mathbf{S}(\mathbf{k})\mathcal{R}^T \mathbf{r}_{3d} - \frac{T_d}{m}\mathbf{S}(\mathbf{k})\mathcal{R}^T \boldsymbol{\delta}\left(\mathbf{e}_1, \mathbf{e}_2\right)\right) \\
=& -W_3(\mathbf{e}_1, \mathbf{e}_2, \mathbf{r}_3, \mathbf{r}_{3d}) \\
& + \mathbf{r}_{3d}^T \mathcal{R}\mathbf{S}(\mathbf{k})\left(\boldsymbol{\omega} - \mathcal{R}^T \mathbf{S}\left(\mathbf{r}_{3d}\right)\dot{\mathbf{r}}_{3d} - k_3 \mathbf{S}(\mathbf{k})\mathcal{R}^T \mathbf{r}_{3d} - \frac{T_d}{m}\mathbf{S}(\mathbf{k})\mathcal{R}^T \boldsymbol{\delta}\left(\mathbf{e}_1, \mathbf{e}_2\right)\right)
\end{aligned} \tag{3.34}$$

where use was made of the fact that $\mathbf{S}\left(\mathbf{r}_3\right) = \mathcal{R}\mathbf{S}\left(\mathbf{k}\right)\mathcal{R}^T$.

Since the control input do not appear yet in the equation, one more error $\mathbf{e}_4$ and respective Lyapunov candidate function are created.

$$\mathbf{e}_4 = \mathbf{S}\left(\mathbf{k}\right)\left(\boldsymbol{\omega} - \mathcal{R}^T \mathbf{S}\left(\mathbf{r}_{3d}\right)\dot{\mathbf{r}}_{3d}\right) - \mathbf{S}\left(\mathbf{k}\right)^2 \mathcal{R}^T \left(k_3 \mathbf{r}_{3d} + \frac{T_d}{m}\boldsymbol{\delta}\left(\mathbf{e}_1, \mathbf{e}_2\right)\right) \tag{3.35}$$

$$V_4 = V_3 + \frac{1}{2}\mathbf{e}_4^T \mathbf{e}_4 \tag{3.36}$$

The time derivative of V_4 gives

$$\begin{aligned}\dot{V}_4 =& \dot{V}_3 + \mathbf{e}_4^T \dot{\mathbf{e}}_4 \\ =& - W_3(\mathbf{e}_1, \mathbf{e}_2, \mathbf{r}_3, \mathbf{r}_{3d}) + \mathbf{r}_{3d}^T \mathcal{R} \mathbf{e}_4 \\ &+ \mathbf{e}_4^T \left(\mathbf{S}(\mathbf{k}) \left(\boldsymbol{\tau} - \frac{\mathrm{d}}{\mathrm{d}t} \left\{ \mathcal{R}^T \mathbf{S}(\mathbf{r}_{3d}) \dot{\mathbf{r}}_{3d} \right\} \right) - \mathbf{S}(\mathbf{k})^2 \frac{\mathrm{d}}{\mathrm{d}t} \left\{ \mathcal{R}^T \left(k_3 \mathbf{r}_{3d} + \frac{T_d}{m} \boldsymbol{\delta}(\mathbf{e}_1, \mathbf{e}_2) \right) \right\} \right)\end{aligned}$$

Computation of these derivatives is not included in the text. However, for the interested reader, they can be found in appendix B.

The remaining input $\boldsymbol{\tau}$ has finally been unveiled and therefore it is now possible to write the final control law.

$$\boldsymbol{\tau} = \frac{\mathrm{d}}{\mathrm{d}t} \left\{ \mathcal{R}^T \mathbf{S}(\mathbf{r}_{3d}) \dot{\mathbf{r}}_{3d} \right\} + \mathbf{S}(\mathbf{k}) \left[k_4 \mathbf{e}_4 + \mathcal{R}^T \mathbf{r}_{3d} + \frac{\mathrm{d}}{\mathrm{d}t} \left\{ \mathcal{R}^T \left(k_3 \mathbf{r}_{3d} + \frac{T_d}{m} \boldsymbol{\delta}(\mathbf{e}_1, \mathbf{e}_2) \right) \right\} \right] + \mathbf{k} \tau_z \quad (3.37)$$

where τ_z corresponds to the third component of τ, and can be arbitrarily set. For the present controller, it was chosen to use it simply to drive ω_z to zero, and therefore

$$\tau_z = -k_z \omega_z \quad (3.38)$$

At this point, the main result of this development is presented

Theorem 3.1. *Let the quadrotor model be described by equation* (3.16) *and consider the control laws* (3.23) *and* (3.37)*, assuming that these are well-defined for all time. Choosing* $k_i > 0$ *renders the origin of the error system asymptotically stable and guarantees global convergence of the tracking error to zero.*

Proof. Substitution of $\boldsymbol{\tau}$ into $\dot{V}_4$ yields

$$\dot{V}_4 = - \begin{bmatrix} \boldsymbol{\sigma}_e^T & \mathbf{e}_2^T \end{bmatrix} \mathbf{Q} \begin{bmatrix} \boldsymbol{\sigma}_e \\ \mathbf{e}_2 \end{bmatrix} - k_3 \mathbf{r}_{3d}^T \mathbf{S}(\mathbf{r}_3)^T \mathbf{S}(\mathbf{r}_3) \mathbf{r}_{3d} - k_4 \mathbf{e}_4^T \mathbf{e}_4 \quad (3.39)$$

which is negative semi-definite, being negative everywhere besides the set $\{\boldsymbol{\sigma}_e = 0, \mathbf{e}_2 = 0, \mathbf{r}_3 = \pm \mathbf{r}_{3d}, \mathbf{e}_4 = 0\}$. Noting that $\boldsymbol{\sigma}_e = 0 \Rightarrow \mathbf{e}_1 + k_2 \mathbf{e}_2 = 0$, having $\mathbf{e}_2 = 0$ imply $\mathbf{e}_1$ to be also zero. This deduction is valid for any initial conditions. Therefore, errors $\mathbf{e}_1$, $\mathbf{e}_2$, and $\mathbf{e}_4$ converge to zero for any initial conditions, meaning that trajectory tracking is achieved globally. □

3.3 Results

This section presents the results of a series of simulations conducted to test the quadrotor controller developed and the integrated strategy for coordinated flight. The vehicles used in the simulations are all equal, weighing $0.1\mathrm{kg}$ and having $J_{xx} = J_{yy} = 1 \times 10^{-3} \mathrm{kg} \cdot \mathrm{m}^2$ and $J_{zz} =$

$2 \times 10^{-3}\mathrm{kg} \cdot \mathrm{m}^2$. These values correspond to a small scale plant similar to the one used in the experimental test of chapter 4. The controller of each quadrotor is configured with the same parameters, which are listed in table 3.1.

Quadrotor controller parameters				
$k_1 = 0.5$	$k_2 = 1.5$	$k_3 = 10$	$k_4 = 0.5$	$k_z = 1$
$\sigma_{\max} = 5$	$c = 50$	$p_{22} = 0.5$	$p_{11} = 1$	$p_{12} = 1/3$

Table 3.1: Configuration parameters of the quadrotor controller.

Quadrotor controller test In the present simulation the quadrotor is set to track a trajectory described by

$$\mathbf{p}_{ref} = \begin{bmatrix} 2\cos(0.25t) \\ \sin(0.5t) \\ -1.5 \end{bmatrix} \tag{3.40}$$

In order to demonstrate the performance of the controller, the quadrotor is initially placed at $\mathbf{p}(0) = [-5\ 10\ -10]^T$, with $\phi(0) = \pi$ and $\psi(0) = 0 = \theta(0)$. The velocities (linear and angular) are initially zero.

Figure 3.2 presents the three-dimensional trajectory of the vehicle with some snapshots of its attitude at the first instants of the simulation. The controller errors are plotted in figure 3.3. Figure 3.4 contains the time evolution of the vehicles velocities – linear (L) and angular (R). Lastly, figure 3.5 plots the vehicles actuation throughout the simulation.

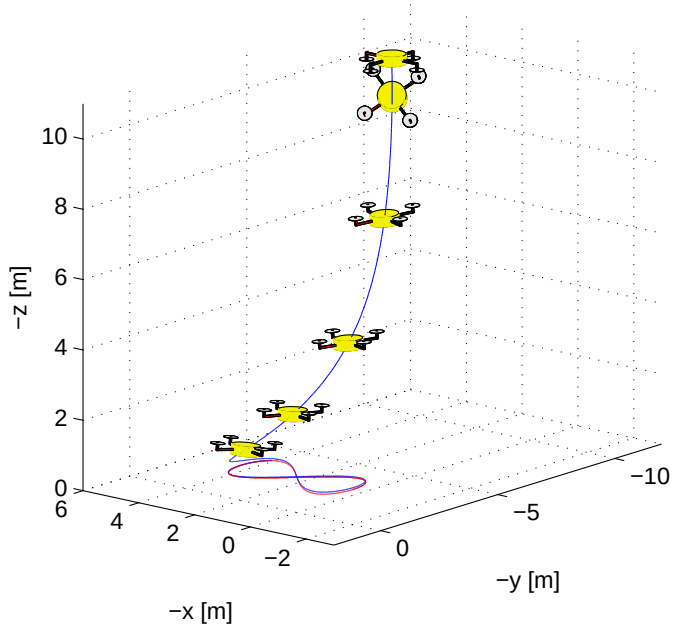

Figure 3.2: Trajectory described by the vehicle (blue), its attitude at initial moment and first 5 seconds, and the reference trajectory (red).

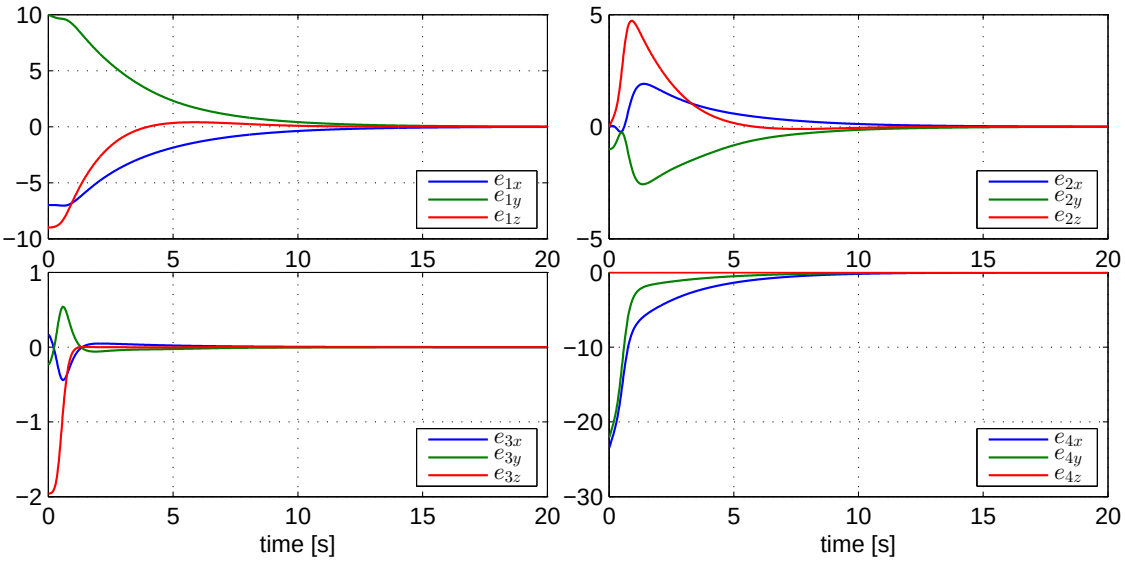

Figure 3.3: Controller errors over time.

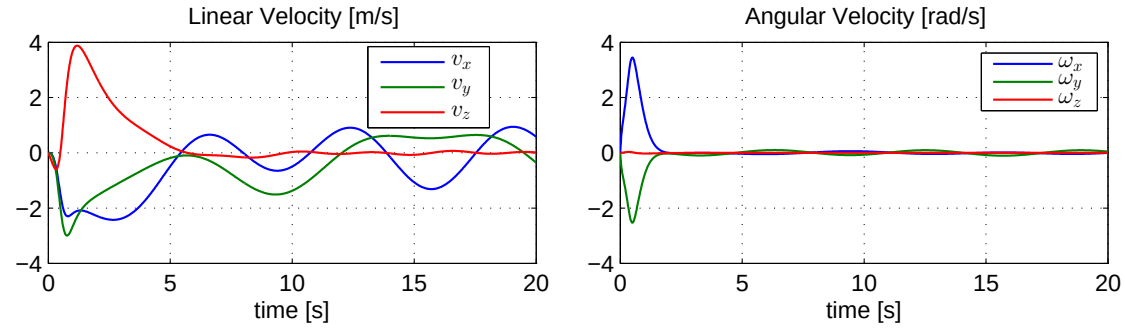

Figure 3.4: Time evolution of linear (L) and angular (R) velocities.

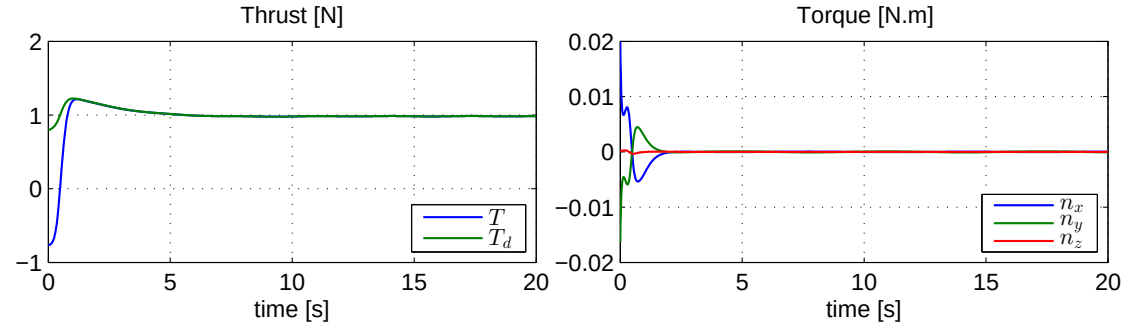

Figure 3.5: Time evolution of thrust and desired thrust (L), and of torques (R).

In this simulation the plant is started in an unfavourable state. Not only is it at a great height and away from the intended trajectory but it is turned upside down. This fact causes the plant to rapidly rotate, as can be observed in figure 3.2 through the snapshots of the plant actuation taken at each second, or in the plot of the error $\mathbf{e}_3$ in figure 3.3 by the rapid evolution of the third component of the error, which indicates an inversion in the direction of the vector $\mathbf{r}_3$. This rapid turn is also noted in the initial evolution of the angular speed (figure 3.4 right).

As can be seen in figure 3.3, the time required for the convergence of the errors is approximately 10 seconds. During the first 1 to 2 seconds a faster convergence of the errors $\mathbf{e}_3$ and $\mathbf{e}_4$ is observed, at the cost of growing the error $\mathbf{e}_2$. The first two errors are the slower to converge and even after $t = 10\text{s}$ a reminiscent error is noticeable, vanishing by the end of the simulation.

As shown in figure 3.5, apart of the initial transient, the actuations do not vary significantly from their nominal values. The large initial difference between the thrust actuation T and its desired value T_d is due to the initial orientation of the vehicle, chosen to generate almost symmetrical thrust direction $\mathbf{r}_3$ and desired thrust direction $\mathbf{r}_{3d}$, and thus leading to a negative initial thrust request.

Quadrotors in formation The results of a simulation with the trajectory planner and the quadrotor controller are now presented. In this simulation the leader, a quadrotor, is set to follow the same trajectory of last simulation, given in equation (3.40). The motion of the leader (position, velocity, and acceleration) is passed to the planner, which generates two different trajectories with identical d_x to be passed as reference to two other quadrotor vehicles. The quadrotors are initially at rest in the floor. Apart from the quadrotor controller gains, already presented in table 3.1, the other parameters, specific of this simulation, are presented in table 3.2.

Configuration	Virtual Controller	
$\mathbf{p}_L(0) = [0 \;\; 0 \;\; 0]^T$		
$\mathbf{p}_{vF1}(0) = [-0.5 \;\; -1 \;\; 0]^T$	$k_1 = 0.2$	$k_2 = 2$
$\mathbf{p}_{vF2}(0) = [-2 \;\; 1 \;\; 0]^T$	$k_3 = 0.5$	$k_{z1} = 0.2$
$\mathbf{d}_1 = [0.35 \;\; 0.35 \;\; -0.3]^T$	$k_{z2} = 2$	$p_{\max} = 5$
$\mathbf{d}_2 = [0.35 \;\; -0.35 \;\; -0.3]^T$	$z_{\max} = 3$	$e_{\max} = 0.4$

Table 3.2: Configuration parameters for the simulated flight formation.

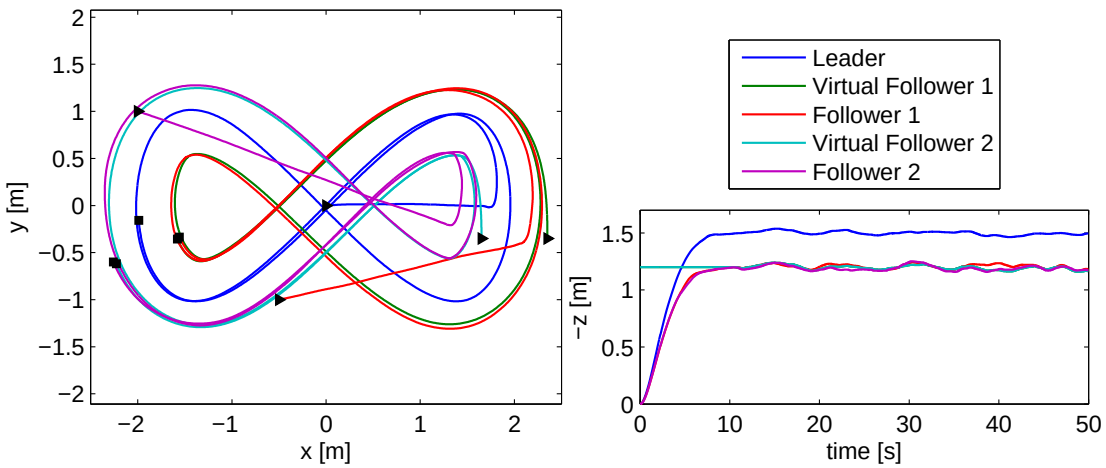

Figure 3.6: Position of the quadrotors, generated trajectories and reference.

To assess the robustness of the coordination strategy, noise was added to the state measure-

ment of each quadrotor. As the trajectory generation depend on the leader's state, the addition of noise to the state indirectly introduces noise in the trajectory generation. The noise added is white and gaussian with zero mean and has a standard deviation of $0.2\mathrm{m}$ for the position, $0.1\mathrm{m/s}$ for the linear velocity, $0.01\mathrm{m/s^2}$ for the acceleration, $0.02°/\mathrm{s}$ for the angular velocity and $0.02°$ for the measurement of the attitude. These values are typical for low cost sensors.

In the planar position plot (see figure 3.6), the symbols ► represent the initial point of each of the vehicles (both quadrotors and virtual followers) and the symbols ■ their positions at the end of the simulation.

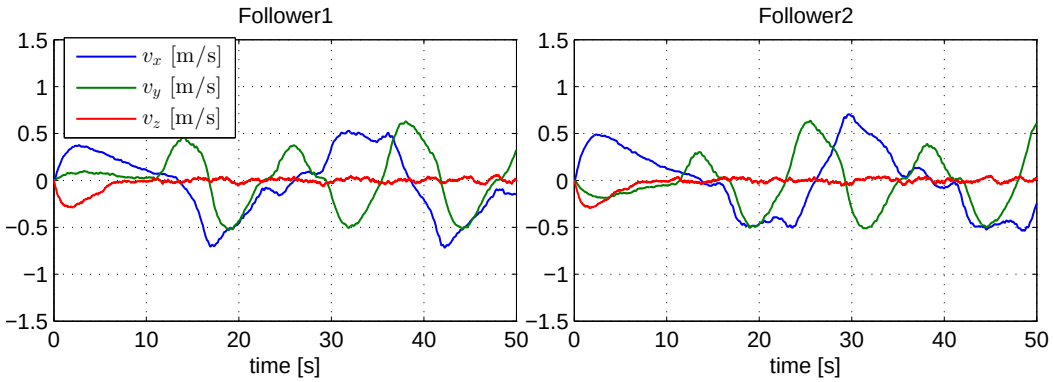

Figure 3.7: Velocity of the followers throughout the simulation.

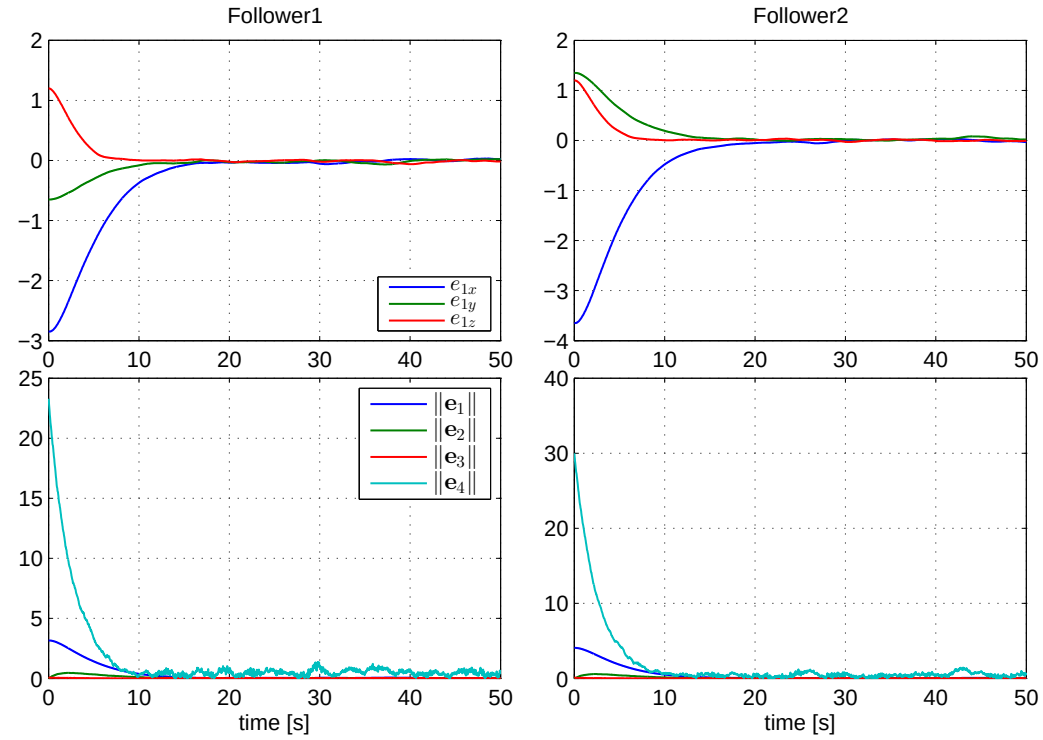

Figure 3.8: Followers errors throughout the simulation.

Figure 3.6 shows that the quadrotors are able to track the trajectories generated by the planner.

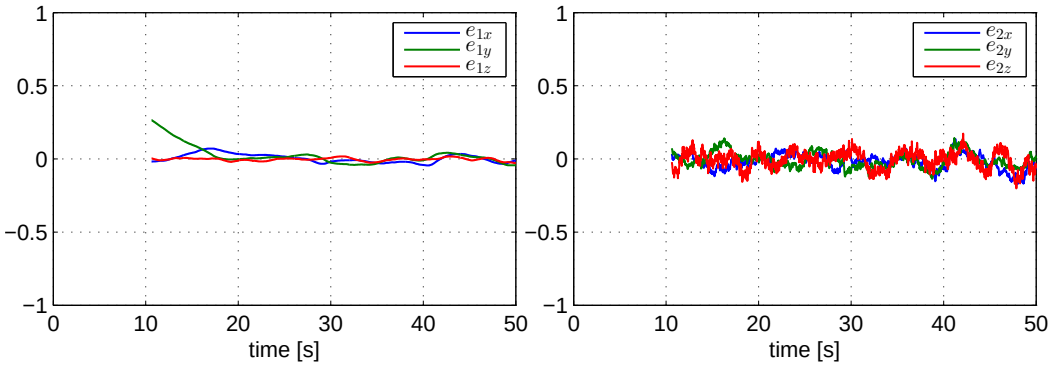

Figure 3.9: Virtual followers errors throughout the simulation.

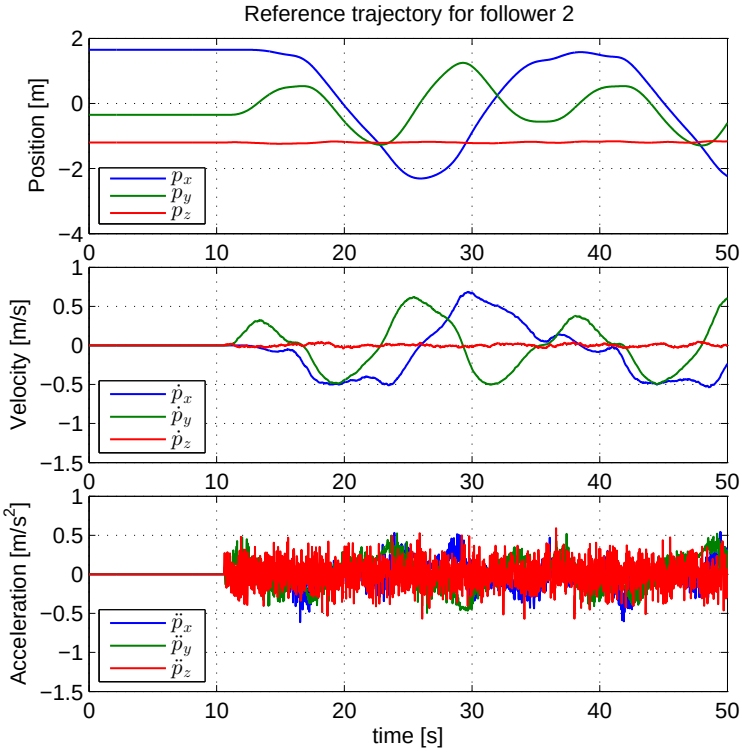

Figure 3.10: Sample trajectory generated (in this case for the second follower).

At the beginning, they rapidly converge to the starting points of the trajectories, while the planner is stopped, as can be observed in figure 3.10. Once they approach these points the planner is finally started and the leader starts describing the eight trajectory.

It is noticeable the effect the noise introduced on the state measurement of the leader has on the trajectory generation. From observation of figure 3.6 (R) one sees that the variations in height of the leader, which were not contained in the reference trajectory, are visible in the height evolution of the followers.

The effect of noise is better noticed in the trajectory generated for the second follower, plotted in figure 3.10. The acceleration is highly contaminated with noise, being difficult to find a visual relation between acceleration an velocity plots.

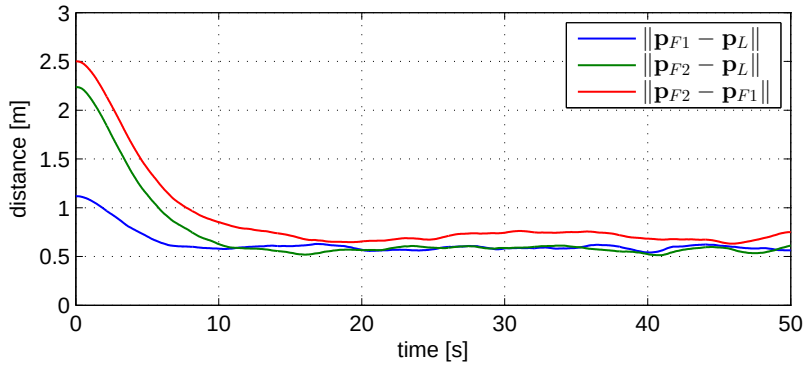

Figure 3.11: Time evolution of distance between leader and followers (and between them).

Lastly, figure 3.11 shows that the distance between quadrotors is kept approximately constant, not varying more than $0.1\mathrm{m}$ between leader and followers and $0.15\mathrm{m}$ between followers, which corresponds to approximately 20% of their average values. It is noticeable a correlation between the variations of these distances and also a higher variation of the distance between the followers, as a result of the noise in trajectory generation.

3.4 Summary

In this chapter, the performance of the trajectory planner in controlling a formation of quadrotors was assessed in simulation. To do so, a model of the plant was built and a trajectory tracking controller was designed.

The simulation carried out to test the controller developed showed that it is capable of steering the quadrotor to the desired trajectory and guarantee an asymptotic tracking, even when started from very unfavourable conditions.

In the simulation to test the planner noise was introduced in the state measurement of each quadrotor. It was noticeable the effect of noise in the generated trajectories and on the tracking of these by the followers. Nevertheless, the quadrotor controllers proved to be robust in tracking the trajectories and in establishing and maintaining the formation.

Chapter 4

Experimental Evaluation

Real world experiments constitute the ultimate stage of validation of any control strategy. Although simulation environments and computer capabilities have evolved enormously, it is not possible to reproduce in simulation the unpredictability of reality.

The present chapter contains the results of a series of experimental tests carried out at the Sensor-Based Cooperative Robotics Research Laboratory – SCORE Lab of the Faculty of Science and Technology at the University of Macau. These tests were conducted using a VICON® system and a group of small scale quadrotor vehicles. A description of the experimental set-up, including a description of the VICON and of the characteristics of the quadrotor used, are provided in section 4.1. Section 4.2 contains the results of some of the experimental tests carried out. Finally, section 4.3 is dedicated to the discussion of the results obtained.

4.1 Experimental Set-up

The laboratory set-up comprises three fundamental parts: a VICON tracking system, two computers, and a set of quadrotors.

The VICON system is responsible for acquiring the motion and attitude of each quadrotor and to send that information to a computer. This computer is running the VICON motion tracking software and the MatLab Simulink®, from MathWorks, with a model containing the planner developed and the quadrotors controllers. The controllers determine the actuation to be applied, which is then sent to another computer through Ethernet. This second computer is responsible for sending the control signals through serial port to a RF module at $44\mathrm{Hz}$.

The decision to separate control and communications was made to avoid jitter in the transmission of the serial-port signals to the RF module. A block diagram of the overall architecture is presented in figure 4.1.

The Simulink model used contains the trajectory planner developed and three quadrotor controllers. These controllers are an adaptation of the one presented in [32] and require the desired

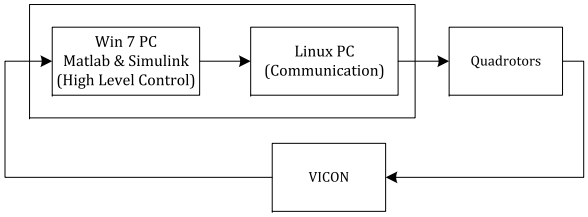

Figure 4.1: System architecture.

position and its derivatives up to the third to be provided. However, in the present test, only position and its first two derivatives were provided.

A block diagram of the Simulink model used in the tests is presented in figure 4.2. Apart from the blocks already referred, it introduces a new block called filter, whose existence is explained in subsection 4.1.3.

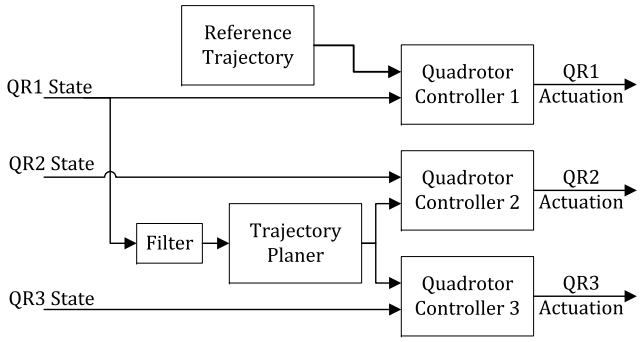

Figure 4.2: Block Diagram of the Simulink model used.

4.1.1 Quadrotor

Quadrotors present several advantages over comparably-scaled helicopters. Quadrotors do not require mechanical linkages to vary the rotor blade pitch angle or to move the tail rotor, which simplifies the vehicle design and reduces maintenance costs [38]. Furthermore, the lift force is distributed by four rotors instead of only one, allowing for smaller rotor diameter, making them safer to operate near humans [35]. They are also easier to model mathematically thus simplifying controller design.

The experimental tests of the present thesis were conducted using three quadrotors Blade mQX®, by Horizon Hobby. This model of quadrotor is an off-the-shelf, ready-to-fly, hobby product, intended to be piloted using a 2.4GHz radio controller. It is highly manoeuvrable, due to its weight, and inexpensive, making it the ideal platform for the present work.

The mQX has an airbourne micro-controller with an inner-loop to stabilise its attitude. It receives commands in terms of thrust T and angular velocity ω.

The vehicles use a 2.4 GHz wideband Direct Sequence Spread Spectrum signal to generate a robust radio link with on-channel interference resistance. This radio technology also allows for the simultaneous use of several vehicles in a confined space, enabling formation flight. The quadrotor vehicles are designed to be human piloted with remote controls but not directly from a computer. In order to be able to send commands to a quadrotor from a computer it was necessary to identify the radio chip inside the remote control and connect the serial interface of the RF module to a computer serial port.

Blade mQX Specifications

Length	353mm
Height	59mm
Propeller Diameter	136mm
Weight	78g

Figure 4.3: The Blade® mQX quadrotor and its specifications.

4.1.2 VICON System

The VICON® is an optical motion capture systems used to track the movement of bodies in space. A variety of successful applications have been reported, from medical, where it has proven to be more effective than clinical examination in evaluating the type of surgery required in children with cerebral palsy [39], or to study physical recovery of patients after surgery [40], to game industry, where it has helped designers to better mimic the movement of humans and thus open the way to more realistic games [41]. Because of its high accuracy [42] it has been used to validate sensors [43]. In recent years, it has been used in laboratories such as GRASP [44] or Flying Machine Arena at IDSC [45] as a way of inertially measuring movements of unmanned air vehicles to validate control strategies [31, 46, 47].

The principle of work of the VICON system consists in recording at a high speed rate the positions of a group of markers installed on the bodies whose movement is of interest to study. Each camera acquires and preprocesses an image, identifying the markers and ruling out the unnecessary information. The preprocessed data is then passed to a centralised workstation which combines the information from each camera, to generate a three dimensional picture of the markers. The number of markers and locations varies depending on the objective of the acquisition. When the objective is to study how a human body behaves while performing certain tasks (see [48], for instance), the markers are installed near articulations, so that a three dimensional point-line picture of the body can be obtained. For rigid bodies, whose configuration does not change, as is

the case of the quadrotors used in this thesis, three markers are sufficient to determine the SO(3) element that fully characterises the quadrotor's position and attitude at any time. The positions of the markers are chosen to maximise their separation and visibility, minimising the errors of estimation.

The experimental tests presented in this thesis were carried out in a laboratory at the University of Macau, which has approximately $3 \times 3 \times 3\mathrm{m}$ of volume. In this laboratory it has been installed recently a VICON Bonita system composed of 12 high speed cameras. Figure 4.4a shows the interior of the lab, while figure 4.4b presents a close-up of one camera there installed. Figure 4.5 is a preview of the data output by the tracking software that accompanies the cameras.

Figure 4.4: The individual camera close-up and laboratory with the cameras installed there.

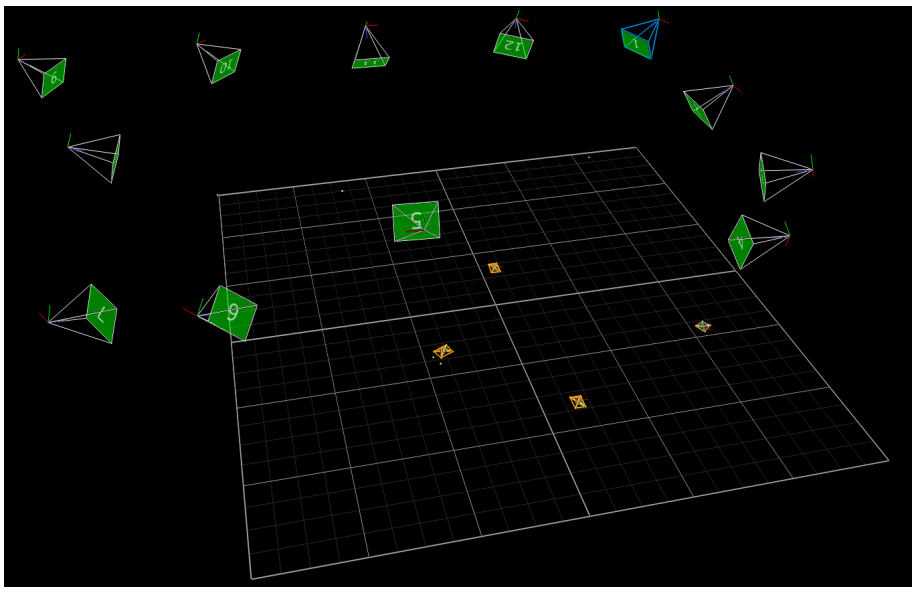

Figure 4.5: A screenshot of the tracking software showing the cameras, their orientation and some vehicles at the centre.

This system is capable of tracking with precision the position and the attitude of various vehicles at the same time at a maximum frame rate of 100 frames per second. However, the greater the frame rate the lower the precision of the system. For that reason, these tests were

conducted at 50 frames per second.

4.1.3 Acceleration estimation

The VICON system outputs a pre-filtered position of the vehicle and with single differences it is possible to obtain a clean estimation of the velocity. However, double differences are highly contaminated with noise, degrading the performance of the estimation. To overcome this problem it is necessary to low-pass filter the VICON measurements.

Filtering introduces phase on signals, degrading speed response of systems. This is particular important when the signal being filtered is part of a control loop, where the filtering process reduces the phase margin of the system. In the current case, however, the measurements being filtered are inputs to the system, not part of the loop, and therefore the impact of delays are diluted. On the other hand, a noisy reference trajectory is undesirable as it results in a generated trajectory polluted with noise.

Using experimental data taken from earlier tests performed with a quadrotor it was possible to test the performance of various filters, with different dimensions. Comparing the performance of a moving average (MAv) filter with the performance of a finite impulsive response (FIR) filter with same number of coefficients (here referred as length) it was concluded that, although the response of the MAv contained more noise, it was less oscillatory, and for that reason the MAv was chosen as the smoothing filter.

After a series of trial and error tests, the final length of the filter was chosen to 100 samples, resulting in a delay of approximately one second. The effect of smoothing with this filter can be observed in figure 4.6, where its application to the double differences of a sample circular trajectory unveils the acceleration of the quadrotor, hidden in the left image.

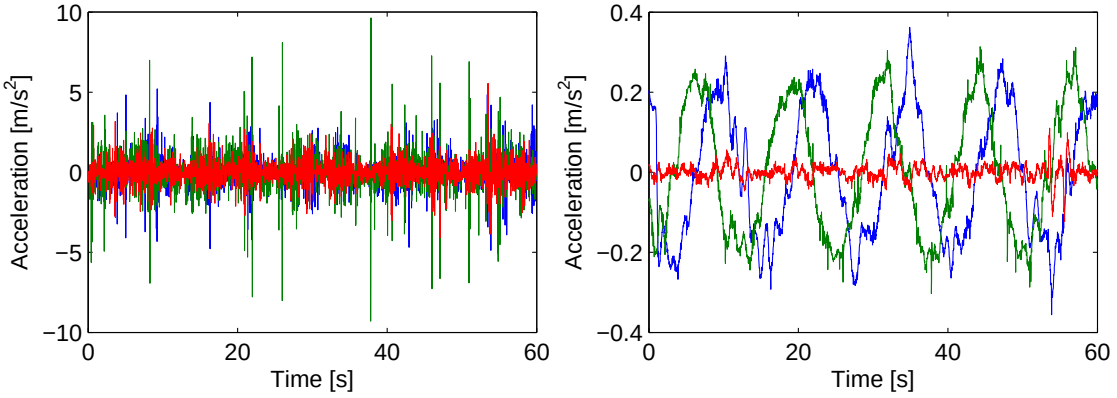

Figure 4.6: Comparison of raw double differences (L) to smoothed with a MAv filter (R) applied to a sample circular trajectory

4.2 Results

A series of experimental test were conducted with the leader tracking different reference trajectories. The table below contains the controllers gains used.

Quadrotor Controller		Virtual Controller	
$k_1 = 1$	$k_2 = 2$	$k_1 = 0.3$	$k_2 = 1.1$
$k_3 = 1.5$	$k_4 = 1$	$k_3 = 0.17$	$k_{z1} = 0.2$
$k_{ang} = 15$	$k_\omega = 1$	$k_{z2} = 1$	$p_{\max} = 5$
$\sigma_{\max} = 2$		$z_{\max} = 3$	$e_{\max} = 0.4$

Table 4.1: Controller parameters used in the experimental tests.

The following paragraphs present the results of some of the tests carried out.

Leader tracking a circumference In this experimental test the leader is tracking a circular reference trajectory given by

$$\mathbf{p}_{ref} = \begin{bmatrix} V_N/\omega_N \cos(\omega_N \gamma) \\ V_N/\omega_N \sin(\omega_N \gamma) \\ -h \end{bmatrix} \tag{4.1}$$

with $\omega_N = 0.5\text{rad/s}$, $V_N = 0.5\text{m/s}$, $h = 1.6\text{m}$. At the beginning of the test the quadrotors are at rest. The leader is at $\mathbf{p}_L(0) = [0.7 \;\; 0.79 \;\; 0]^T$, follower 1 at $\mathbf{p}_{F1}(0) = [-0.18 \;\; 0.71 \;\; 0]^T$ and follower 2 at $\mathbf{p}_{F2}(0) = [-0.13 \;\; 1.43 \;\; 0]^T$. The vectors $\mathbf{d}$ for each follower were $\mathbf{d}_1 = [0.35 \;\; 0.35 \;\; -0.3]^T$ and $\mathbf{d}_2 = [0.35 \;\; -0.35 \;\; -0.3]^T$.

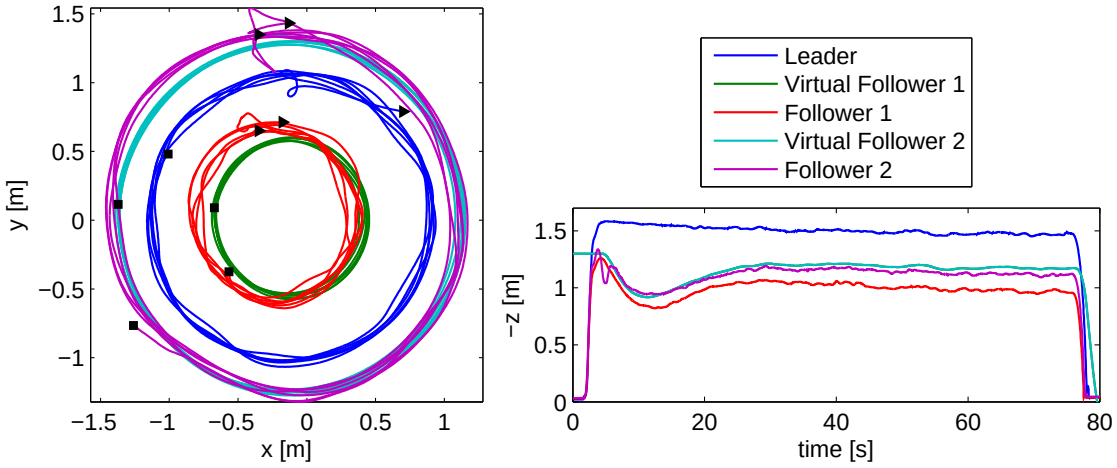

Figure 4.7: Position of the leader, generated trajectories and respective followers.

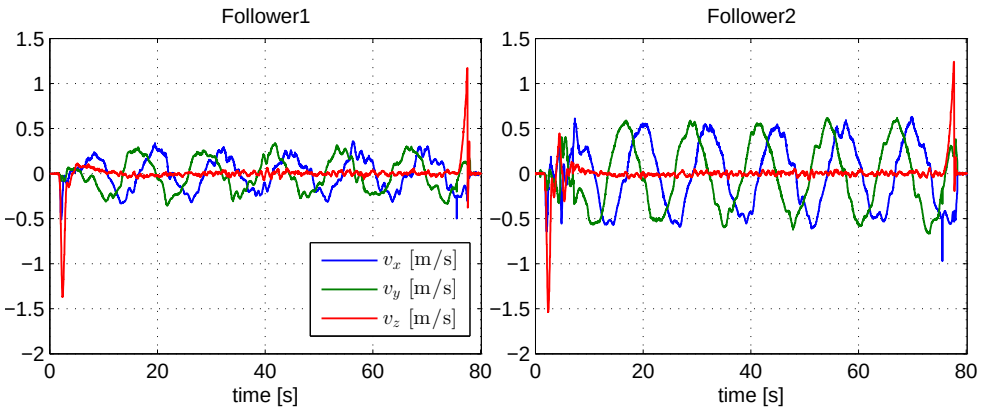

Figure 4.8: Time evolution of velocities of both the followers.

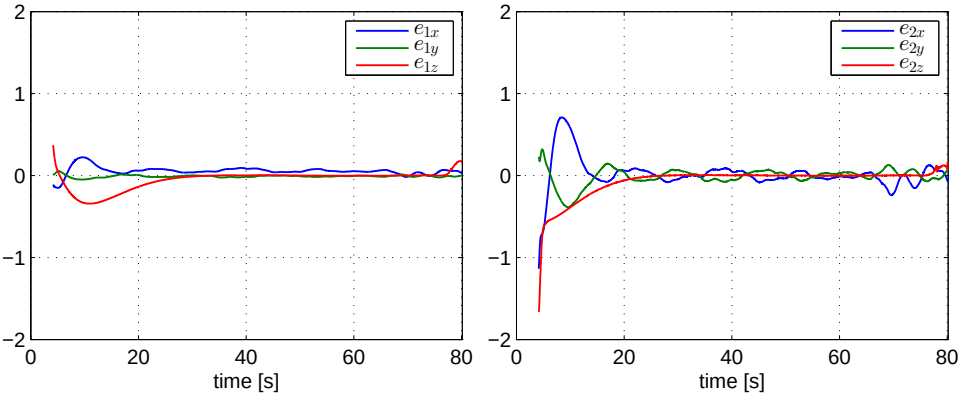

Figure 4.9: Time evolution of the errors for both the virtual followers.

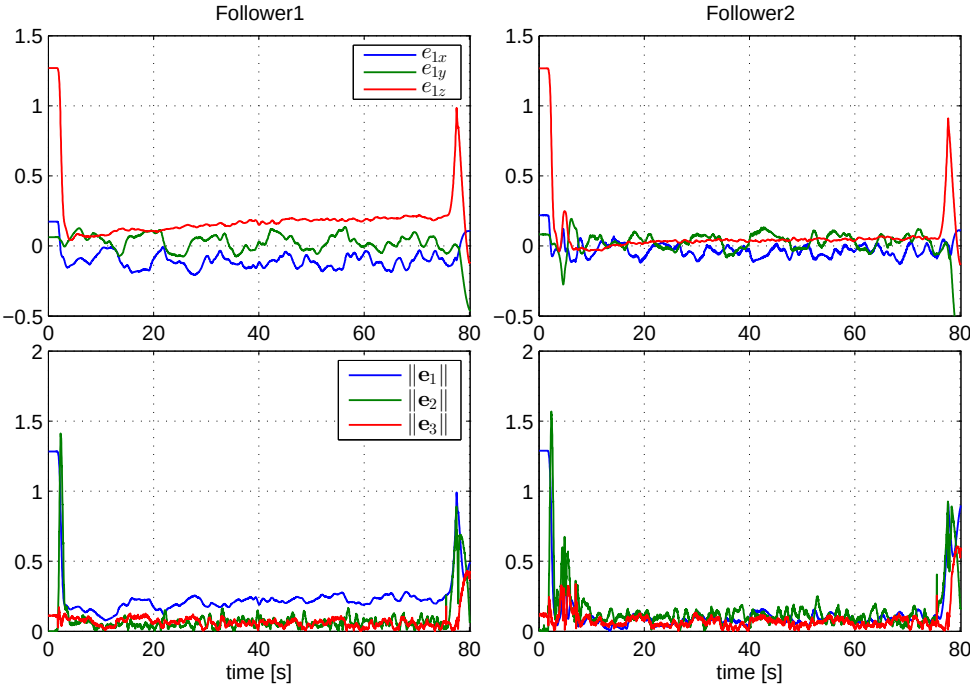

Figure 4.10: Time evolution of controller errors for both the followers.

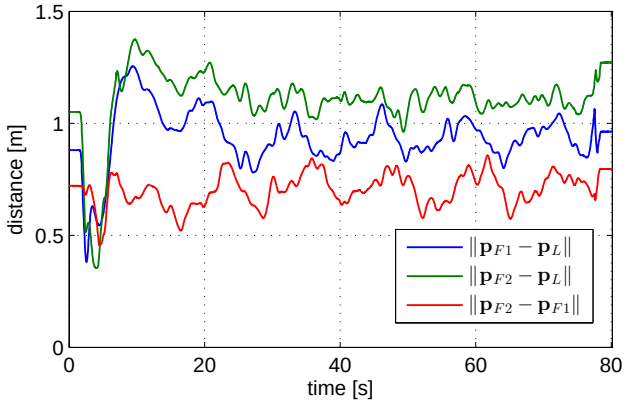

Figure 4.11: Time evolution of distance between leader and followers (and between them).

Leader tracking an eight In this experimental test the leader is tracking a lemniscate curve of the Bernoulli type. This curve is similar to the eight-figure introduced in equation (2.35), which is also a lemniscate curve, but of Gerono. The reason for the choice of trajectory is the fact that the lemniscate of Bernoulli has less variation of curvature, being possible to reduce its dimensions more than the other, still avoiding inversions in virtual followers' directions of movement. The present lemniscate curve is mathematically given by

$$\mathbf{p}_{ref} = \begin{bmatrix} \dfrac{V_N}{\omega_N} \dfrac{\cos(\omega_N \gamma)}{\sin^2 \omega_N \gamma + 1} \\ \dfrac{V_N}{\omega_N} \dfrac{\sin(2\omega_N \gamma)}{\sin^2 \omega_N \gamma + 1} \\ -h \end{bmatrix} \tag{4.2}$$

with $\omega_N = 2/3\text{rad/s}$, $V_N = 0.5\text{m/s}$ and $h = 1.6\text{m}$. The parameter γ was used to rectify the trajectory speed and hence is given by

$$\dot{\gamma} = \sqrt{1 + \sin^2 \gamma} \tag{4.3}$$

In order to better use the space available in the laboratory the reference trajectory was rotated by $\pi/4$ counter-clockwise and translated by $[0\ 0.5\ 0]^T$.

At the beginning of the test the quadrotors are at rest. The leader is at $\mathbf{p}_L(0) = [-1\ \ 0.48\ \ 0]^T$, follower 1 at $\mathbf{p}_{F1}(0) = [-0.57\ \ -0.37\ \ 0]^T$ and follower 2 at $\mathbf{p}_{F2}(0) = [-1.26\ \ -0.77\ \ 0]^T$. The vectors $\mathbf{d}$ for each follower were $\mathbf{d}_1 = [0.35\ \ 0.35\ \ -0.3]^T$ and $\mathbf{d}_2 = [0.35\ \ -0.35\ \ -0.3]^T$.

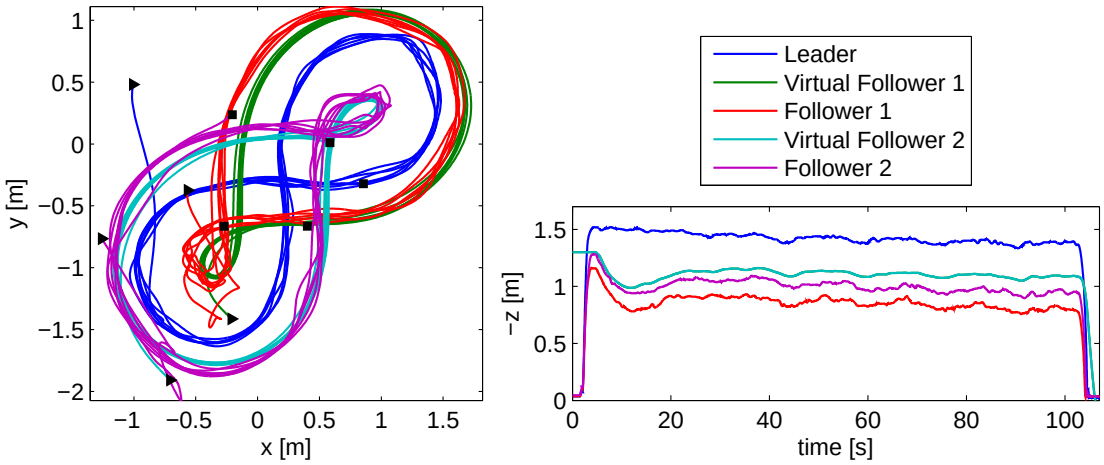

Figure 4.12: Position of the leader, generated trajectories and respective followers.

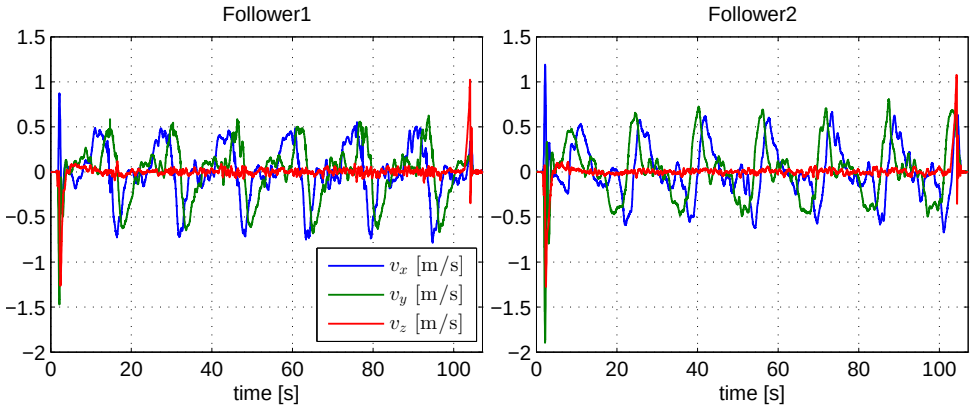

Figure 4.13: Time evolution of velocities of both the followers.

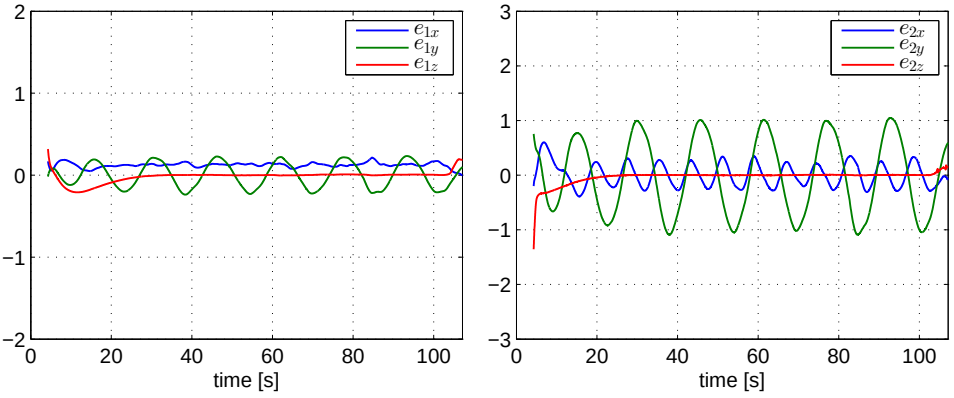

Figure 4.14: Time evolution of errors for both the virtual followers.

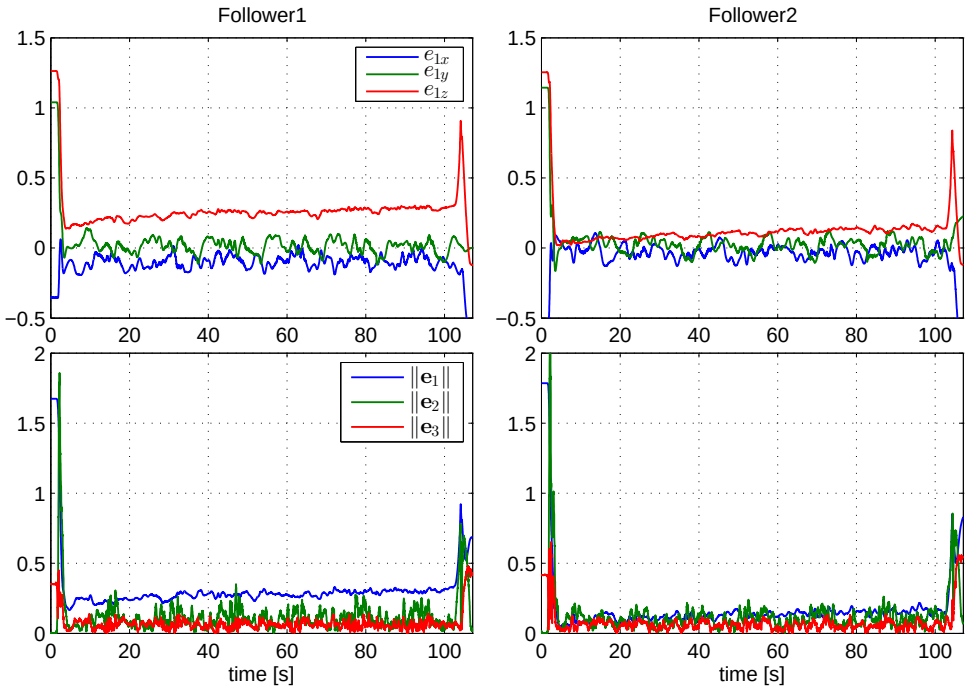

Figure 4.15: Time evolution of controller errors for the both followers.

Leader tracking a square In this experimental test the leader is tracking a smooth square reference trajectory, continuous in position and velocity. This trajectory cannot be defined by a simple equation and therefore is presented in a graphical form in figure 4.16.

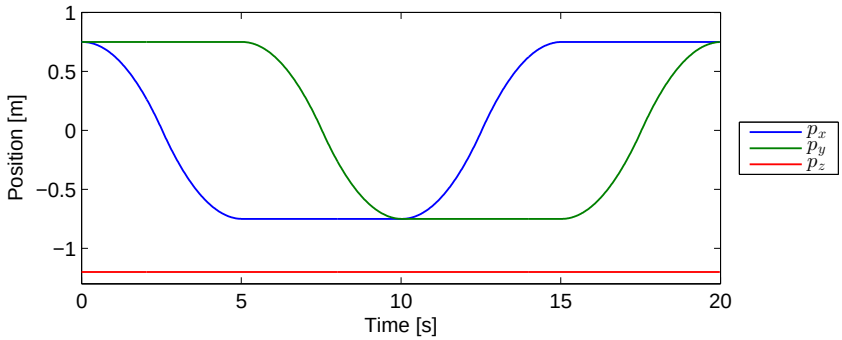

Figure 4.16: Time evolution of square reference trajectory (a complete track).

Because of the sharp corners, this experiment was conducted with only one follower, moving outside the square described by the leader, thus avoiding inversions in its direction of movement.

At the beginning of the test the quadrotors are at rest. The leader is at $\mathbf{p}_L(0) = [0.63 \quad -0.54 \quad 0]^T$ and the follower at $\mathbf{p}_F(0) = [0.31 \quad -1.05 \quad 0]^T$. The vector $\mathbf{d}$ for this test is $\mathbf{d} = [0.35 \quad 0.35 \quad -0.3]^T$.

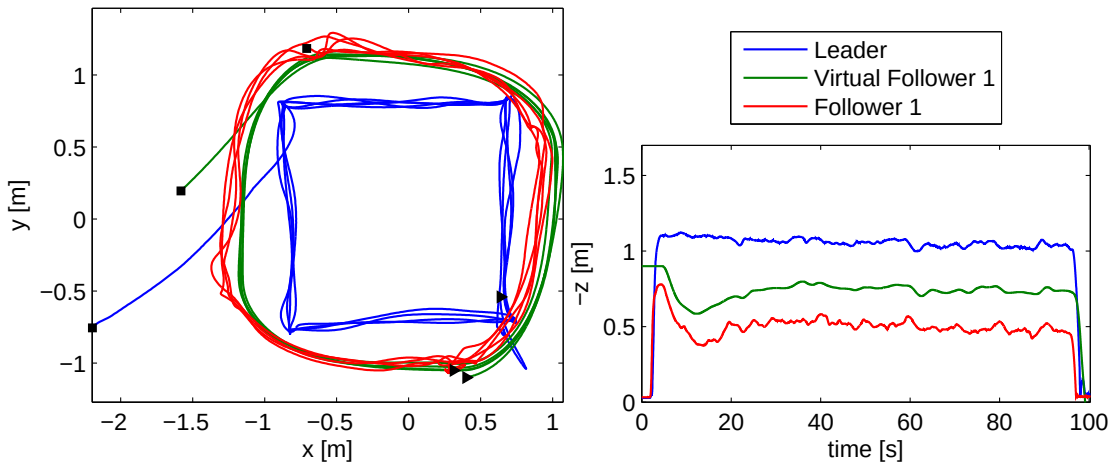

Figure 4.17: Position of the leader, generated trajectory and respective follower.

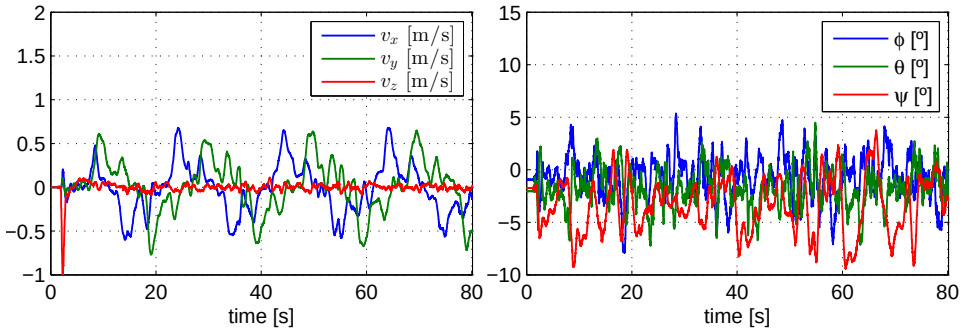

Figure 4.18: Time evolution of velocities and Euler angles of the follower.

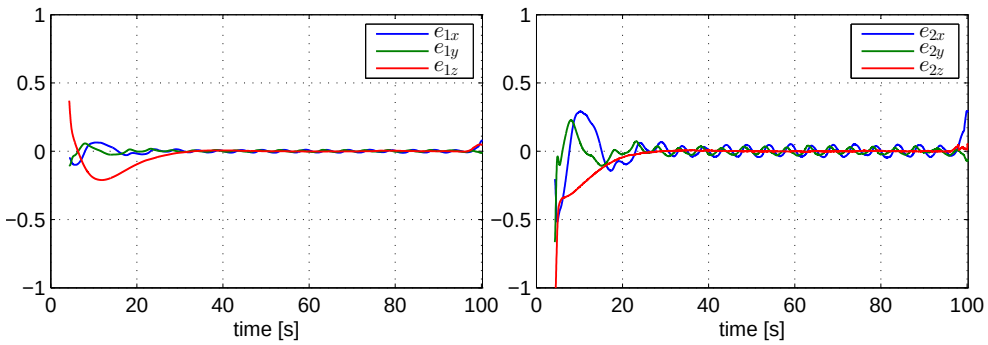

Figure 4.19: Time evolution of errors for the virtual follower.

4.3 Discussion

At the beginning of the tracking, i.e. when the quadrotors approach the intended initial positions, a loss of height is observed both in the virtual and real followers (see for example figure 4.7 right). This might be caused by an overshoot in the response of the virtual controllers to an apparent lower vertical position of the leader, as a result of the delay introduced by the smoothing

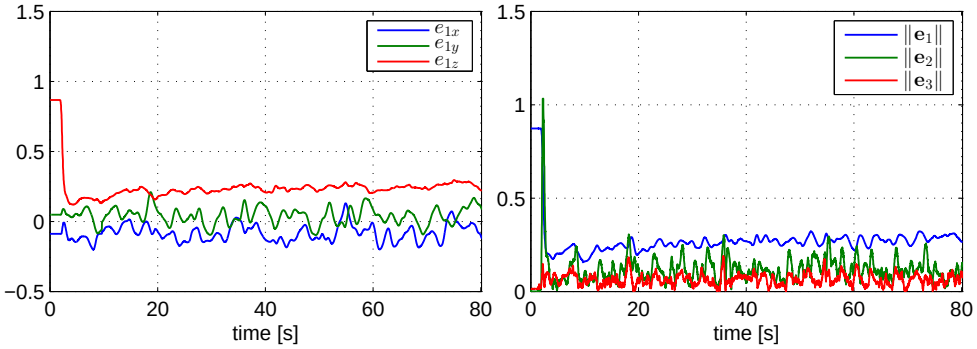

Figure 4.20: Time evolution of controller errors for the follower.

process. This overshoot is reduced in subsequent tests, by adjusting the gains of the vertical controller. However, it could not be eliminated. The gains required to do so make the controller too sensitive to the vertical oscillations of the leader.

One other effect of smoothing is the apparent smaller dimensions of the figures described by the leader. In figure 4.7, for example, although the value of $|d_y|$ is the same for both the followers, the follower describing the inner circumference has apparently a greater value of $|d_y|$ than the outer vehicle. In fact, both have the same d_y (apart from the sign) but both see the leader describing a smaller circle. A similar effect is observed in figure 4.12.

Nevertheless, it is the use of smoothing that makes it possible to generate trajectories for the followers that are not greatly affected by the noise which contaminates the double differences applied to VICON measurements. The effect of the smoothing can be plainly seen in the trajectories generated with contrast to the one described by the leader. The reader is invited to see figure 4.12 right, for example, and notice the similarity between the dark blue line and the light blue one. The longer and slower variations found in the leader's height can also be found in the height of the virtual followers (the green line cannot be seen for being shadowed by the light blue one). On the other hand, the more instantaneous changes in leader's height are filtered and do not appear in the generated trajectory. The result are smooth trajectories that the following quadrotors are capable of tracking without much oscillatory effects, as can be observed in position plots of figures 4.7 and 4.12 or, more clearly, in the velocity plots of figures 4.8 and 4.13, for example.

The reader may have noticed that only the errors of one virtual follower are plotted for each test (figures 4.9 and 4.14). That is because they are equal. In fact, since the virtual followers are started with the same orientation and with null errors in relation to the reference trajectories and since they are subjected to exactly the same noise (the noise contained in leader's trajectory), the evolution of the errors is the same.

From observation of figures 4.9, 4.19, but especially of figure 4.14, it is possible to identify an oscillatory behaviour on the virtual errors. This oscillation is a result of the gain trade-off found between mitigation of virtual error $\mathbf{e}_1$ and limiting the sensitiveness of the trajectories to the perturbations in leader's movement. It is possible to maintain the virtual errors close to the origin,

but at the cost of degrading the performance of the following quadrotors.

Figure 4.11 plots the time evolution of the distance between the leader and the followers (and between the followers). It is noticeable the less oscillatory behaviour of the distance between the leader and the second follower (green line). The more oscillatory behaviour of the other lines is caused by the movement of the first follower which, as can be seen by comparing images on top of figure 4.10, is more varying and seems to exhibit a similar pattern (the same period) to what is found in blue and red curves of figure 4.11. Although oscillatory, the distance between the followers oscillates around $0.7\mathrm{m}$ (as expected from the values of d_y of both followers), with a course of approximately $0.2\mathrm{m}$.

Chapter 5

Conclusions

This thesis addressed the problem of motion coordination between autonomous vehicles. Its main contribution was the development of a trajectory planner that can be used to coordinate the movement of any type of autonomous vehicles.

The planner consists of a group of virtual vehicles (one per each following vehicle) whose objective is to maintain a predefined relative position to the leader. These virtual vehicles are modelled as nonholonomic cars and are controlled using a nonlinear controller, designed through a backstepping procedure. Expressing the controller errors in the body frame allowed to concentrate the actuation in a vector, resulting in a simple control law that guarantees global and asymptotic stability of the origin of the error system, as demonstrated in the text.

Nevertheless, stability of the errors does not guarantee stability of the intrinsic variables of a vehicle. An analysis of the inner dynamics showed that it is in fact stable and, if some limits on the parameters of the trajectory described by the leader and on the configuration of each follower are respected, the evolution of the intrinsic variables is deterministic, although difficult to determine. These limits relate the longitudinal desired distance from each follower to the leader to the instantaneous radius of rotation of the trajectory. When the longitudinal distance between leader and follower is much greater than the radius of rotation of the leader's trajectory, the intrinsic variables tend to be slow variant, which is in accordance with the intuition of a distant observer trying to follow an apparently stopped leader. Conversely, when the opposite holds, the trajectories of both tend to be much similar. The boundary between these two behaviours occurs when the longitudinal distance between leader and follower is approximately equal to the instantaneous radius of rotation of the leader's trajectory.

It is possible to limit the speed variation of the followers by carefully choosing the trajectory parameters and follower configuration. This possibility might be of particular importance when generating trajectories for vehicles such as aircrafts, for which a minimum speed is imposed.

When the followers share the same longitudinal distance, the formation moves as if it was rigidly connected. Each follower has a definite position within the formation which is fixed with

respect to a local frame attached to the followers. This behaviour is unique of this strategy and is a result not only of the objective imposed – maintain a relative position to the leader – but also of the vehicle model chosen for the virtual followers. A different choice of virtual vehicle with the same control objective would result in a different formation behaviour.

The performance of the planner in coordinating the movement of a group of quadrotor vehicles was assessed in simulation. To do so, a simulation model of the quadrotor was built and a trajectory tracking controller developed. The model describes the plant as being actuated in terms of thrust, aligned with the vertical axis, and in terms of torque, in all directions. The controller employs the concept of desired thrust and desired thrust direction to drive the position and velocity to the desired ones. Convergence of the actual thrust and thrust direction to the desired is guaranteed by a control law derived using the backstepping procedure. The influence of position and velocity on the actuation is limited by a saturation function introduced in the control law. As simulations demonstrated, this controller is capable of steering the plant to the desired trajectory, even when started in unfavourable conditions.

The simulation of the coordination demonstrated the validity of the concept. One quadrotor was set to track a reference trajectory and its state passed to the planner which generated the trajectories for another two vehicles. To better emulate a real situation, noise was added to the state measurement of each quadrotor. This caused a degradation in the performance of the overall system. Nevertheless, both the planner and the quadrotor controller proved to be robust to disturbances.

The experimental evaluation conducted corroborate the results obtained in simulation, demonstrating that the planner can be effectively used to coordinate the flight of multiple aerial vehicles. The strategy was tested with the leader tracking a variety of trajectories from circles to squares. Although only the position could be measured, estimates of velocity and acceleration could be obtained successfully by single and double differencing the measurements followed by smoothing. The result were smooth trajectories that could easily be tracked by the quadrotors.

5.1 Future Work

Every work has a start but hardly any work has an end. This thesis presented the concept of a leader-following technique for coordinated motion of multiple vehicles but its possibilities have only been grasped.

The nature of movement presented by the followers is in part caused by the characteristics of the model chosen to describe the virtual vehicles. This fact suggests that the use of different vehicle models is likely to produce new motion characteristics of interest to be exploited. Therefore, part of the future effort shall be directed at investigating other vehicle models with potential to bring about new features to the planner.

A capability the planner is still lacking is collision avoidance. Implementing such capability

constitute one important topic for future work. One possible way towards that objective would be to explore the concept of virtual leaders developed in [23]. As was noted in the introductory part of this text, with this strategy the shape of the formation is controlled by the movement of the virtual leaders. Using the planner developed to generate the movement of these virtual leaders it is possible to force the formation to move in the same way, thus preserving the properties of the planner whilst taking advantage of the collision avoidance capability provided by the other strategy.

Concerning the experimental tests, although it was demonstrated the validity of the concept, there is plenty of space for improvement. One critical part of the experiments is the motion estimation of the leader, which influences the motion of other vehicles. In that sense, it is a direction of future work to improve the motion estimation performance, either through the use of more effective algorithms and/or through the inclusion of other sensors.

To summarise, the directions of future work include:

- explore other possibilities of virtual vehicle models;
- develop collision avoidance capabilities for the planner;
- improve and optimise the motion estimation.

Appendix A

Trajectory Analysis

The curvature of the planar projection of the trajectory described by the leader is of key importance to the analysis of the trajectories attained by the following virtual vehicles. This appendix is dedicated to the determination of a general expression for the curvature and particularising it for the case of the eight trajectory.

Consider a curve in a two-dimensional space given by

$$\mathbf{p}(\xi) = \begin{bmatrix} \mathbf{p}_x(\xi) & \mathbf{p}_y(\xi) \end{bmatrix}^T \tag{A.1}$$

where $\xi \in \mathbb{R}$ is the scalar variable that parametrises the curve. The length of the curve over the domain $[\xi_0,\ \xi]$ is called arc-length and is given by

$$s(\xi) = \int_{\xi_0}^{\xi} \left\| \frac{\mathrm{d}\mathbf{p}}{\mathrm{d}\tau}(\tau) \right\| d\tau \tag{A.2}$$

The direction of the curve at each point, that is, the direction of the line tangent to the curve at each point is represented by $\theta(\xi)$ and is given by

$$\theta(\xi) = \arctan\left(\frac{p'_y(\xi)}{p'_x(\xi)}\right) \tag{A.3}$$

where the apostrophe denotes the derivative with respect to ξ.

The curvature is defined as the derivative of the direction with respect to the arc-length:

$$\kappa(\xi) = \frac{\mathrm{d}\theta}{\mathrm{d}s}(\xi) = \frac{\dfrac{\mathrm{d}\theta}{\mathrm{d}\xi}}{\dfrac{\mathrm{d}s}{\mathrm{d}\xi}} = \frac{\dfrac{1}{1 + p'^2_y/p'^2_y}\left(\dfrac{p''_y}{p'_x} - \dfrac{p'_y p''_x}{p'^2_x}\right)}{\sqrt{p'^2_x + p'^2_y}} = \frac{p''_y p'_x - p'_y p''_x}{\left(p'^2_x + p'^2_y\right)^{3/2}} \tag{A.4}$$

when the trajectory is parametrised by time the curvature might be written as function of the

angular and linear speeds of the curve:

$$\kappa(t) = \frac{\dfrac{\mathrm{d}\theta}{\mathrm{d}t}}{\dfrac{\mathrm{d}s}{\mathrm{d}t}} = \frac{\omega}{V} \tag{A.5}$$

A.1 Eight Trajectory

The time evolution of the leader's planar position on an eight shape trajectory is defined in equation (2.35) as

$$\mathbf{p}_L = \begin{bmatrix} \dfrac{V_N}{\omega_N}\cos(\omega_N t) \\ \dfrac{V_N}{2\omega_N}\sin(2\omega_N t) \end{bmatrix}$$

where V_N and ω_N are the nominal values of linear and angular speeds, respectively. The velocity and acceleration result straightforwardly from time derivation of the above expression.

The curvature of this trajectory can be obtained with recourse to equation (A.4).

$$\kappa_L = \frac{2\sin\omega_N t\sin 2\omega_N t + \cos\omega_N t\cos 2\omega_N t}{\left(\sin^2\omega_N t + \cos^2 2\omega_N t\right)^{3/2}}\kappa_N \tag{A.6}$$

The time evolution of the resulting equation is plotted in figure A.1.

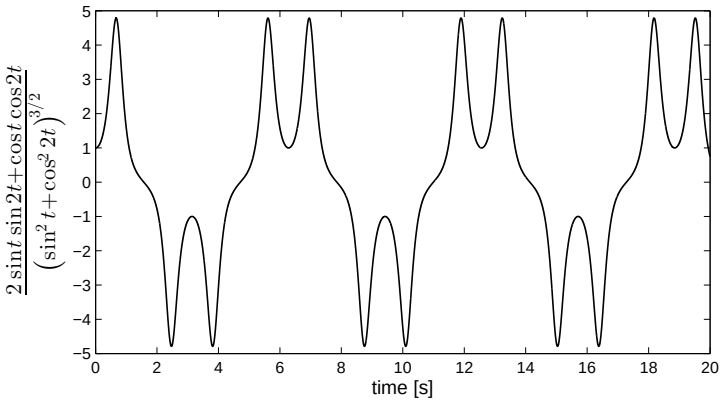

Figure A.1: Evolution of κ_L for a nominal value of κ_N.

The maximum value of κ_L is easily found numerically, showing that it is a linear function of κ_N.

$$\begin{aligned} |\kappa_L|_{\max} =& \kappa_N \left| \frac{2\sin\omega_N t\sin 2\omega_N t + \cos\omega_N t\cos 2\omega_N t}{\left(\sin^2\omega_N t + \cos^2 2\omega_N t\right)^{3/2}} \right|_{\max} \\ \approx& 4.79\kappa_N \end{aligned} \tag{A.7}$$

Appendix B

Quadrotor Controller – Complementary Mathematic

The present appendix contains additional mathematical deductions used to implement in simulation the quadrotor controller developed.

The first derivative of (3.39) may be developed as:

$$\frac{\mathrm{d}}{\mathrm{d}t}\left\{\mathcal{R}^T\mathbf{S}\left(\mathbf{r}_{3d}\right)\dot{\mathbf{r}}_{3d}\right\} = -\mathbf{S}(\boldsymbol{\omega})\mathcal{R}^T\mathbf{S}\left(\mathbf{r}_{3d}\right)\dot{\mathbf{r}}_{3d} + \mathcal{R}^T\mathbf{S}\left(\mathbf{r}_{3d}\right)\ddot{\mathbf{r}}_{3d} \tag{B.1}$$

Let $\mathbf{d}_3$ be an auxiliary variable given by

$$\mathbf{d}_3 = g\mathbf{u}_3 - \ddot{\mathbf{p}}_d + \boldsymbol{\sigma}_e \tag{B.2}$$

which allows the desired thrust and desired thrust direction to be written as

$$T_d = m\|\mathbf{d}_3\| \qquad\qquad \mathbf{r}_{3d} = \frac{\mathbf{d}_3}{\|\mathbf{d}_3\|}$$

Making use of these redefinitions $\ddot{\mathbf{r}}_{3d}$ is given by

$$\begin{aligned}\ddot{\mathbf{r}}_{3d} =& \frac{\mathrm{d}^2}{\mathrm{d}t^2}\mathbf{r}_{3d}\\ =& \frac{\mathrm{d}}{\mathrm{d}t}\left\{-\mathbf{S}\left(\mathbf{r}_{3d}\right)^2\frac{\dot{\mathbf{d}}_3}{\|\mathbf{d}_3\|}\right\}\\ =& -\mathbf{S}\left(\dot{\mathbf{r}}_{3d}\right)\mathbf{S}\left(\mathbf{r}_{3d}\right)\frac{\dot{\mathbf{d}}_3}{\|\mathbf{d}_3\|} - \mathbf{S}\left(\mathbf{r}_{3d}\right)\mathbf{S}\left(\dot{\mathbf{r}}_{3d}\right)\frac{\dot{\mathbf{d}}_3}{\|\mathbf{d}_3\|} - \mathbf{S}\left(\mathbf{r}_{3d}\right)^2\left(\frac{\ddot{\mathbf{d}}_3}{\|\mathbf{d}_3\|} - \frac{\dot{\mathbf{d}}_3\dot{\mathbf{d}}_3^T}{\|\mathbf{d}_3\|^3}\mathbf{d}_3\right)\end{aligned} \tag{B.3}$$

where,

$$\ddot{\mathbf{d}}_3 = \frac{\mathrm{d}^2}{\mathrm{d}t^2}\left\{g\mathbf{u}_3 - \ddot{\mathbf{p}}_d + \boldsymbol{\sigma}_e\right\} = \mathbf{p}_d^{(4)} + \ddot{\boldsymbol{\sigma}}_e \tag{B.4}$$

The other derivative of equation (3.39) can be developed in the following way:

$$\begin{aligned}
&\frac{\mathrm{d}}{\mathrm{d}t}\left\{\mathcal{R}^T\left(k_3\mathbf{r}_{3d}+\frac{T_d}{m}\boldsymbol{\delta}\left(\mathbf{e}_1,\mathbf{e}_2\right)\right)\right\}\\
&\quad=-\mathbf{S}(\omega)\mathcal{R}^T\left(k_3\mathbf{r}_{3d}+\frac{T_d}{m}\boldsymbol{\delta}\left(\mathbf{e}_1,\mathbf{e}_2\right)\right)+\mathcal{R}^T\frac{\mathrm{d}}{\mathrm{d}t}\left\{k_3\mathbf{r}_{3d}+\frac{T_d}{m}\boldsymbol{\delta}\left(\mathbf{e}_1,\mathbf{e}_2\right)\right\}\\
&\quad=-\mathbf{S}(\omega)\mathcal{R}^T\left(k_3\mathbf{r}_{3d}+\frac{T_d}{m}\boldsymbol{\delta}\left(\mathbf{e}_1,\mathbf{e}_2\right)\right)+\mathcal{R}^T\left(k_3\dot{\mathbf{r}}_{3d}+\frac{T_d}{m}\dot{\boldsymbol{\delta}}\left(\mathbf{e}_1,\mathbf{e}_2\right)+\frac{\dot{T}_d}{m}\boldsymbol{\delta}\left(\mathbf{e}_1,\mathbf{e}_2\right)\right)
\end{aligned}\tag{B.5}$$

where,

$$\dot{T}_d=m\mathbf{d}_3^T\dot{\mathbf{d}}_3$$

$$\dot{\boldsymbol{\delta}}\left(\mathbf{e}_1,\mathbf{e}_2\right)=k_2p_{12}\frac{\mathrm{d}\boldsymbol{\sigma}_e'}{\mathrm{d}t}\left(\frac{k_2}{k_1}\boldsymbol{\sigma}_e+\mathbf{e}_2\right)+k_2p_{12}\boldsymbol{\sigma}_e'\left(\frac{k_2}{k_1}\dot{\boldsymbol{\sigma}}_e+\dot{\mathbf{e}}_2\right)+\left(k_2-p_{12}\right)\dot{\boldsymbol{\sigma}}_e+k_1\dot{\mathbf{e}}_2$$

Bibliography

[1] J. K. Parrish and L. Edelstein-Keshet, “Complexity, pattern, and evolutionary trade-offs in animal aggregation,” *Science*, vol. 284, no. 5411, pp. 99–101, 1999.

[2] C. Cutts and J. Speakman, “Energy savings in formation flight of pink-footed geese,” *Journal of Experimental Biology*, vol. 189, no. 1, pp. 251–61, 1994.

[3] S. Sariel, T. Balch, and N. Erdogan, “Naval mine countermeasure missions,” *Robotics Automation Magazine, IEEE*, vol. 15, pp. 45 –52, march 2008.

[4] M. Kovacina, D. Palmer, G. Yang, and R. Vaidyanathan, “Multi-agent control algorithms for chemical cloud detection and mapping using unmanned air vehicles,” in *Intelligent Robots and Systems, 2002. IEEE/RSJ International Conference on*, vol. 3, pp. 2782 – 2788 vol.3, 2002.

[5] A. Sarlette, R. Sepulchre, and N. Leonard, “Cooperative attitude synchronization in satellite swarms: a consensus approach,” *Proceedings of the 17th IFAC Symposium on Automatic Control in Aerospace*, 2007.

[6] H. Cho and F. E. Udwadia, “Explicit solution to the full nonlinear problem for satellite formation-keeping,” *Acta Astronautica*, vol. 67, pp. 369 – 387, 2010.

[7] W. Sheng, Q. Yang, J. Tan, and N. Xi, “Distributed multi-robot coordination in area exploration,” *Robotics and Autonomous Systems*, vol. 54, no. 12, pp. 945 – 955, 2006.

[8] D. Nowak, I. Price, and G. Lamont, “Self organized uav swarm planning optimization for search and destroy using swarmfare simulation,” in *Simulation Conference, 2007 Winter*, pp. 1315 –1323, dec. 2007.

[9] Y. Altshuler, V. Yanovsky, I. a. Wagner, and A. m. Bruckstein, “Efficient cooperative search of smart targets using uav swarms1,” *Robotica*, vol. 26, pp. 551–557, July 2008.

[10] P. Dasgupta, S. O Hara, and P. Petrov, “A multi-agent uav swarm for automatic target recognition,” in *Defence Applications of Multi-Agent Systems* (S. Thompson and R. Ghanea-Hercock, eds.), vol. 3890 of *Lecture Notes in Computer Science*, pp. 80–91, Springer Berlin / Heidelberg, 2006.

[11] J. Corner and G. Lamont, “Parallel simulation of uav swarm scenarios,” in *Simulation Conference, 2004. Proceedings of the 2004 Winter*, vol. 1, december 2004.

[12] S. Waharte, N. Trigoni, and S. Julier, “Coordinated search with a swarm of uavs,” in *Sensor, Mesh and Ad Hoc Communications and Networks Workshops, 2009. SECON Workshops ’09. 6th Annual IEEE Communications Society Conference on*, pp. 1 –3, june 2009.

[13] N. Miyata, J. Ota, T. Arai, and H. Asama, “Cooperative transport by multiple mobile robots in unknown static environments associated with real-time task assignment,” *Robotics and Automation, IEEE Transactions on*, vol. 18, pp. 769 – 780, oct 2002.

[14] P. Chamoun and M. Lanthier, “Rigorous movement of convex polygons on a path using multiple robots,” 2012.

[15] N. Michael, J. Fink, and V. Kumar, “Cooperative manipulation and transportation with aerial robots,” *Autonomous Robots*, vol. 30, pp. 73–86, january 2011.

[16] R. Olfati-Saber, “Flocking for multi-agent dynamic systems: algorithms and theory,” *Automatic Control, IEEE Transactions on*, vol. 51, pp. 401 – 420, march 2006.

[17] E. Justh and P. Krishnaprasad, “Equilibria and steering laws for planar formations,” *Systems and Control Letters*, vol. 52, no. 1, pp. 25 – 38, 2004.

[18] D. S. Morgan and I. B. Schwartz, “Dynamic coordinated control laws in multiple agent models,” *Physics Letters A*, vol. 340, no. 1-4, pp. 121–131, 2005.

[19] J. Guerrero and R. Lozano, “Flight formation of multiple mini rotorcraft based on nested saturations,” in *Intelligent Robots and Systems (IROS), 2010 IEEE/RSJ International Conference on*, pp. 634 –639, oct. 2010.

[20] S. A. Ning, *AIRCRAFT DRAG REDUCTION THROUGH EXTENDED FORMATION FLIGHT*. PhD thesis, Stanford University, 2011.

[21] M. T. Morgan, “A study in drag reduction of close formation flight accounting for flight control trim positions and dissimilar formations,” Master’s thesis, Air Force Institute of Technology, Air University, 2005.

[22] C. Wikipedia, “V formation.” `http://en.wikipedia.org/wiki/V_formation`, August 2012.

[23] N. Leonard and E. Fiorelli, “Virtual leaders, artificial potentials and coordinated control of groups,” in *Decision and Control, 2001. Proceedings of the 40th IEEE Conference on*, vol. 3, pp. 2968 –2973 vol.3, 2001.

[24] C. Wikipedia, “Nonholonomic system.” `http://en.wikipedia.org/wiki/Nonholonomic_system`, August 2012.

[25] A. D. Luca, G. Oriolo, A. De, and C. Samson, “Feedback control of a nonholonomic car-like robot,” 1997.

[26] P. Kokotović and M. Arcak, “Constructive nonlinear control: a historical perspective,” *Automatica*, vol. 37, no. 5, pp. 637 – 662, 2001.

[27] P. Kokotovic, “The joy of feedback: nonlinear and adaptive,” *Control Systems, IEEE*, vol. 12, pp. 7 –17, june 1992.

[28] R. Skjetne and T. I. Fossen, “On integral control in backstepping: Analysis of different techniques,” in *Proceedings of the American Control Conference*, pp. 1899 – 1904, 2004.

[29] J. G. Leishman, *Principles of Helicopter Aerodynamics*. Cambridge University Press, 2000.

[30] S. Newman, *The foundations of helicopter flight*. Halsted Press, 1994.

[31] M. S. Daniel Mellinger and V. Kumar, “Control of quadrotors for robust perching and landing,” *International Powered Lift Conference*.

[32] D. Cabecinhas, R. Cunha, and C. Silvestre, “Rotorcraft path following control for extended flight envelope coverage,” in *Decision and Control, 2009 held jointly with the 2009 28th Chinese Control Conference. CDC/CCC 2009. Proceedings of the 48th IEEE Conference on*, pp. 3460 –3465, dec. 2009.

[33] V. de Brederode, *Fundamentos de Aerodinâmica Incompressível*. Author, 1997.

[34] G. D. Padfield, *Helicopter flight dynamics : the theory and application of flying qualities and simulation modelling*. Blackwell Publishing, 2 ed., 2007.

[35] G. M. Hoffmann, H. Huang, S. L. Wasl, and E. C. J. Tomlin, “Quadrotor helicopter flight dynamics and control: Theory and experiment,” in *In Proc. of the AIAA Guidance, Navigation, and Control Conference*, 2007.

[36] R. Cunha, D. Cabecinhas, and C. Silvestre, “Nonlinear trajectory tracking control of a quadrotor vehicle,” in *Proceedings of the European Control Conference*, 2009.

[37] K. B. Petersen, M. S. Pedersen, J. Larsen, K. Strimmer, L. Christiansen, K. Hansen, L. He, L. Thibaut, M. Barão, S. Hattinger, V. Sima, and W. The, “The matrix cookbook,” tech. rep., 2006.

[38] P. Pounds, R. Mahony, and P. Corke, “Modelling and control of a large quadrotor robot,” *Control Engineering Practice*, vol. 18, no. 7, pp. 691 – 699, 2010.

[39] E. Lee, J. Goh, and K. Bose, “Value of gait analysis in the assessment of surgery in cerebral palsy..”.

[40] D. Bennett, L. Ogonda, D. Elliott, L. Humphreys, and D. Beverland, “Comparison of gait kinematics in patients receiving minimally invasive and traditional hip replacement surgery: A prospective blinded study,” *Gait and Posture*, vol. 23, no. 3, pp. 374 – 382, 2006.

[41] K. Mackinder and S. Fleming, “Vicon leads market for motion capture in games.” urlhttp://www.sourcewire.com/news/24649/vicon-leads-market-for-motion-capture-in-games, August 2012.

[42] M. Windolf, N. G´otzen, and M. Morlock, “Systematic accuracy and precision analysis of video motion capturing systems exemplified on the vicon-460 system,” *Journal of Biomechanics*, vol. 41, no. 12, pp. 2776 – 2780, 2008.

[43] J. D. Hol and M. Elzinga, “’uwb/imu tracking validation using an optical system’.”.

[44] “Grasp laboratory.” `https://www.grasp.upenn.edu/`, August 2012.

[45] “The flying machine arena.” `http://www.idsc.ethz.ch/Research_DAndrea/FMA/`, August 2012.

[46] A. K. B. K. V. K. Caitlin Powers, Daniel Mellinger, “Influence of aerodynamics and proximity effects in quadrotor flight.” 12th International Symposium on Experimental Robotics, 2012.

[47] G. Ducard and R. D’Andrea, “Autonomous quadrotor flight using a vision system and accommodating frames misalignment,” in *Industrial Embedded Systems, 2009. SIES ’09. IEEE International Symposium on*, pp. 261 –264, july 2009.

[48] M. J. R. C. G. A. Nancy S. Pollard, Jessica K. Hodgins, “Adapting human motion for the control of a humanoid robot,” in *Robotics and Automation, Proceedings of the 2002 IEEE International Conference on*, pp. 1390 – 1397, 2002.